

---

# Numerical Simulations of the Flow in the HYPULSE Expansion Tube

---

Gregory J. Wilson, Myles A. Sussman, and  
Robert J. Bakos

---

June 1995



National Aeronautics and  
Space Administration

---

# Numerical Simulations of the Flow in the HYPULSE Expansion Tube

---

Gregory J. Wilson, Myles A. Sussman, and Robert J. Bakos, Thermosciences Institute,  
Ames Research Center, Moffett Field, California

June 1995



National Aeronautics and  
Space Administration

**Ames Research Center**  
Moffett Field, CA 94035-1000

# Numerical Simulations of the Flow in the HYPULSE Expansion Tube

GREGORY J. WILSON,\* MYLES A. SUSSMAN,\* AND ROBERT J. BAKOS\*\*

*Thermosciences Institute*

## Summary

Axisymmetric numerical simulations with finite-rate chemistry are presented for two operating conditions in the HYPULSE expansion tube. The operating gas for these two cases is nitrogen and the computations are compared to experimental data. One test condition is at a total enthalpy of 15.2 MJ/Kg and a relatively low static pressure of 2 kPa. This case is characterized by a laminar boundary layer and significant chemical nonequilibrium in the acceleration gas. The second test condition is at a total enthalpy of 10.2 MJ/Kg and a static pressure of 38 kPa and is characterized by a turbulent boundary layer. For both cases, the time-varying test gas pressure predicted by the simulations is in good agreement with experimental data. The computations are also found to be in good agreement with Mirels' correlations for shock tube flow. It is shown that the nonuniformity of the test gas observed in the HYPULSE expansion tube is strongly linked to the boundary layer thickness. The turbulent flow investigated has a larger boundary layer and greater test gas nonuniformity. In order to investigate possibilities of improving expansion tube flow quality by reducing the boundary layer thickness, parametric studies showing the effect of density and turbulent transition point on the test conditions are also presented. Although an increase in the expansion tube operating pressure level would reduce the boundary layer thickness, the simulations indicate that the reduction would be less than what is predicted by flat plate boundary layer correlations.

## Introduction

The expansion tube was proposed by Trimpi (1962, 1965, and 1966) as a method of achieving higher total pressure, higher enthalpy test conditions than can be provided using other types of ground testing facilities. Figure 1 depicts the components and ideal operating sequence of an expansion tube using an x-t diagram. It is composed of the

following three sections: a driver, a driven section (containing the test gas), and an acceleration section. The operation of the expansion tube begins by rupturing a diaphragm separating the driver gas from the test gas. An incident shock wave travels into the test gas, compressing it. At the end of the intermediate tube, the incident shock ruptures a second diaphragm. This creates a second incident shock and a second expansion, both of which travel down the acceleration tube. The secondary expansion propagates upstream with respect to the test gas but is convected downstream in the supersonic flow. The unsteady expansion of the test gas creates the high velocity test conditions at the exit of the acceleration tube. The test gas is typically air; however, the expansion tube has also recently proved useful for unique experiments which accelerate combustible mixtures to high velocities (Srulijes, et al., 1992 and Kamel, et al., 1995).

It can be argued that the full potential of the expansion tube has yet to be demonstrated and that the primary deficiency is non-ideal flow in the acceleration tube caused by turbulent boundary layers. The turbulent boundary layer thickness can become significant compared to the tube radius even when using a relatively short acceleration tube because the acceleration tube fill pressures are typically low. A thick boundary layer creates axial nonuniformity in the inviscid portion of the flow, or core flow, as well as reducing the amount of core flow available for testing. Although the boundary layer thickness at the exit can be reduced by decreasing the length of the acceleration tube, this reduces the test time.

The negative impact of the acceleration tube boundary layer has been demonstrated in the operational experience with the HYPULSE expansion tube. In spite of the fact that the expansion tube can theoretically provide an infinite set of test conditions by properly setting the fill pressures in the intermediate and acceleration tubes, there has been difficulty in finding acceptable test conditions in HYPULSE. This particular expansion tube was operated at NASA Langley in the 1960s and 1970s. During that time, essentially only one test point was used. This condition is now called the Langley test condition and is characterized by a relatively low static pressure and a laminar boundary layer. Subsequent experimental activities with this facility after it was moved to General Applied Science

---

\* Ames Research Center, Moffett Field, California.

\*\* General Applied Science Laboratories, Inc., Ronkonkoma, New York.

Laboratory (GASL) have increased the number of test points. One of the main guidelines used to find other acceptable conditions has been to avoid the transition of the boundary layer from laminar to turbulent flow during the test time (Erdos, et al., 1994). Unfortunately, test conditions which follow this guideline and have a fully turbulent boundary layer during the test time result in significant nonuniformity of the test gas and less-than-desirable core flow diameter.

One of the primary effects of the boundary layer on shock tube and expansion tube flow is the departure of the shock and interface speeds from inviscid predictions. This is illustrated in the x-t diagram of shock tube flow in figure 2(a). It is seen that the shock speed decreases (attenuates) compared to the inviscid shock speed and the interface speed increases. After traveling a sufficient distance, the shock and interface reach the same speed. Thereafter, the separation distance remains constant at a limiting value,  $l_m$ . In inviscid flow, the separation distance continues to increase linearly with time. Figure 2(b) contains a schematic diagram of the major features of shock tube flow with a boundary layer in laboratory coordinates. There is a large body of analysis, mostly due to Mirels (1963, 1964, 1966, and 1971), which explains and quantifies the boundary layer growth between the shock and the interface (region 1) as well as the shock attenuation and interface acceleration discussed in figure 2(a). However, this theory offers little detailed information about the effect of the boundary layer growth on the expanded driver gas (region 2). Part of the difficulty in characterizing this region is the presence of both driver gas and driven gas in the boundary layer. For many shock tube flows, a detailed understanding of the expanded gas is not required since the driven gas (region 1) is the region of interest. In an expansion tube, the expanded intermediate tube gas (region 2) is the primary region of interest. Computational fluid dynamics (CFD) simulations can provide information about both regions and can therefore be an important tool for studying expansion tube flow. In addition, CFD simulations can incorporate the effects of thermochemical nonequilibrium and turbulent transition which are not included in Mirels' analysis.

Axisymmetric CFD simulations of expansion tube flow were first performed by Jacobs (1992). He computed the transient flow in the HYPULSE facility throughout the complete operating cycle starting from the main diaphragm rupture. The simulations used an explicit numerical scheme on fixed grids. The computed flow-fields were compared to experiments which used helium (to avoid chemistry effects) and had a laminar boundary layer. Several of the sources of noise in expansion tube flows were studied using the numerical simulations. Unlike the previous work, the present approach uses a

moving grid and an implicit treatment of viscous terms in the Navier–Stokes equations, thereby allowing for significantly smaller grid spacing at the wall and better resolution of the boundary layer. This permits the modeling of turbulence. In addition, multiple species continuity equations are included in the present formulation allowing experiments with nitrogen to be simulated including finite rate chemistry.

The CFD code used in this work has been previously used to compute the flow in a reflected shock tube to investigate how the interaction of the reflected shock with the boundary layer can reduce test time (Wilson, et al., 1993). It has also been used to compare computed laminar boundary layer growth in a shock tube with Mirels' analysis (Sharma and Wilson, 1995). This latter study demonstrated the difficulty of achieving a grid independent solution for shock tube flows. One of the primary challenges is the large disparity in length scales between the boundary layer and flow features traversing a facility meters in length. The previous work showed that with the proper grid, results in close agreement with Mirels' correlations can be achieved. This provides confidence in applying CFD methodology to flows where Mirels' analysis cannot be used.

The present work investigates two of the operating conditions commonly used in the HYPULSE expansion tube. One of the cases, referred to as the Mach 17 condition, produces a 15.2 MJ/Kg test gas and a laminar boundary layer during the test time (it is similar to the Langley test condition mentioned above). The other case, referred to as the Mach 14 High Pressure (HP) test condition, produces a 10.2 MJ/Kg test gas and a turbulent boundary layer during the test time. The major goal of the present research is to better characterize the test gas conditions in the HYPULSE facility and more confidently explain the cause of experimentally observed test gas nonuniformity. This not only allows for improved accuracy in interpretation of data but may also lead to ideas to enhance expansion tube flow quality. Another goal of this research is to better establish requirements for accurate numerical simulations of high enthalpy ground test facilities.

## Description of Numerical Algorithm

The flow through the expansion tube is modeled using the thin layer Navier–Stokes equations for a chemically reacting ideal gas mixture. The present gas model includes three gas species, although only two species ( $N_2$  and  $N$ ) are required to simulate the selected experiments. The present formulation also includes a separate vibrational energy equation so that vibrational non-equilibrium can be modeled with a single vibrational temperature; how-

ever, the present computations are specified to be in thermal equilibrium. Species diffusion is not included in the present model.

The axisymmetric gas dynamic equations are solved using an explicit finite-volume form of the Harten–Yee upwind TVD scheme (Yee, 1989). The simulations cluster grid points at the shock and interface and translate this clustered grid with these features to minimize numerical errors. The solutions are advanced at a Courant–Friedrichs–Lewy (CFL) number of less than one based on the inviscid gas dynamics. In the boundary layer this CFL number can be larger than the stability bound required by the viscous terms. To avoid limiting the time step due to the viscous terms, these terms are treated implicitly. This required a block tri-diagonal matrix inversion along each line of cells normal to the wall. The cost of this inversion is more than offset by the larger allowable time step. Simple numerical experiments in which the time step was successively decreased suggest the implicit treatment of the viscous terms does not significantly reduce the time accuracy of the numerical scheme. The source terms representing the finite-rate chemical kinetics and vibrational relaxation are also treated implicitly. The moving grid and single step implicit algorithm reduces the formal time accuracy to first order.

The internal energies for the gas species are computed from statistical mechanics including anharmonic corrections and the first electronic states. The forward reaction rate for nitrogen dissociation is taken from Park (1993). The equilibrium constant is computed using curve fits developed by GASL which extend to 24,000 K. The viscosity and thermal conductivity coefficients are obtained using the curve fits found in Gupta, et al. (1990).

The turbulence model employed is the algebraic model for compressible flow proposed by Cebeci and Smith (1974). This model was adopted, rather than the Baldwin–Lomax model (1978), because finding the edge of the boundary layer as required by the Cebeci–Smith model was more straightforward than finding the maximum in vorticity as required by the Baldwin–Lomax model. The computed vorticity values in the area around the interface were not smooth, making the implementation of the Baldwin–Lomax model difficult. In addition, the compressibility factor in the Cebeci–Smith model which applies local values of density and viscosity seems more appropriate in the test gas region where the boundary layer is comprised of both acceleration and driven tube gas. A modification of the intermittency factor in the Cebeci–Smith model as proposed by Shirazi and Truman (1989) for hypersonic flow was also tried but gave worse agreement with the experimental data. Therefore, all the present results use the original Cebeci–Smith model.

## Computational Domain and Adaptive Grid Solution Procedure

The physical domain of the present simulations is shown in figure 3. It includes only the driven and acceleration tubes and is initialized with the driven tube incident shock and the appropriate post-shock conditions. A no slip, fixed temperature boundary condition is applied at the wall. The shock is initially located several meters upstream of the secondary diaphragm and there is no boundary layer. Since the post-shock flow is supersonic in the laboratory frame, the inflow is also set to the post-shock conditions. This particular initial condition was adopted to avoid the expense of adding the driver section, but it also introduces several approximations. A more accurate implementation of the inflow conditions would include time-varying boundary layer and core flow. The effect of this approximation on the present results was investigated by performing computations with the initial shock location at different distances upstream of the secondary diaphragm and also by computing one case with inviscid flow in the driven tube. These computations produced some variation in the solution compared to the baseline results primarily because of driven tube shock attenuation. A possibly more important simplification of the initial conditions is the absence from the simulation of the primary driver-driven gas interface, which is a consequence of not including the driver section. The head of the secondary rarefaction can interact with the primary interface and produce reflected waves which can travel back into the test gas (Shinn and Miller, 1976). It is believed that the test gas of the particular cases simulated here is not affected by this phenomenon but subsequent research should include this effect. In addition, the computations do not include geometric details of the primary diaphragm station, which were identified by Jacobs (1992) as a potentially significant source of noise.

The grid spacing normal to the wall is held fixed throughout the simulation. The grid spacing in the axial direction, however, is allowed to vary. The motion is controlled to position fine axial spacing around the shock and interface and to place an even finer axial spacing at the secondary diaphragm at the time of rupture. Since the shock is captured by the numerical method (rather than fitted), the finer grid spacing around the shock results in a thinner shock and better resolution of the boundary layer just behind the shock. The finer grid at the interface reduces numerical diffusion. The fine axial spacing at the diaphragm at rupture is required to accurately capture the evolution of the Riemann problem associated with the large pressure and temperature ratios across the diaphragm. The choice of grid spacing at the diaphragm is

guided by experience with one-dimensional (1-D) simulations (Wilson, 1992).

The axial grid motion is shown in the schematic diagram in figure 4. A cluster of finely spaced grid lines is placed around the initial shock position in the driven tube and an even finer grid clustering is placed around the secondary diaphragm location (fig. 4(a)). Approximately one half of the axial grid points are allocated to each side of the diaphragm. As the driven tube shock moves down the tube, the clustered grid translates with it (fig. 4(b)). Near the secondary diaphragm, the clustered grid associated with the shock moves up against the fine grid at the diaphragm and is stopped (fig. 4(c)). The shock is allowed to proceed over the fixed mesh until the diaphragm location is reached and the diaphragm is ruptured. The diaphragm rupture is simulated by resetting the cells in the acceleration tube from the driven tube fill conditions to the acceleration tube fill conditions, thereby creating the secondary shock and interface (fig. 4(d)). As the interface begins to move, the fine grid is translated with it while the secondary shock is allowed to proceed across the grid points clustered around the diaphragm. Since the shock is moving faster than the interface, the number of points between the shock and interface increases with time. Once a specified number of points are located between the interface and shock, the fine grid near the shock is moved with it, as was done in the driven tube (fig. 4(e)). After this time, the number of points between the shock and interface remains the same. Superimposed with the grid motion just described is the gradual expansion of the grid spacing near the interface so that it becomes similar to the grid spacing at the shock (i.e., from 5  $\mu\text{m}$  at diaphragm rupture to a final value of 350  $\mu\text{m}$ ).

### **Mach 17 HYPULSE Test Condition**

Although the Mach 17 condition is normally obtained with air in the intermediate and acceleration tubes, several calibration experiments using nitrogen in both tubes have been performed. The experiments using nitrogen are considered here, to reduce the cost of the numerical simulations. The reported initial conditions and test gas conditions are given in tables 1 and 2, respectively. A 14.62 m acceleration tube is used for the Mach 17 test condition giving a length to diameter (L/D) ratio of approximately 96. There is some complexity in comparing the CFD simulations to the experimental data because the initial conditions used for the simulations differ slightly from the conditions used in the experiments. The difference occurred because the simulations were done before the experimental results were made available. The initial conditions for the computations are given in table 3.

tables 1 and 3 indicate that the experimental values for the driven tube shock speed and acceleration tube fill pressure are 2880 m/sec and 6.0 Pa, respectively, while the computational values are 2665 m/sec and 7.2 Pa. To quantify the difference in acceleration tube conditions that might be expected from the different initial conditions, secondary shock properties were computed from both sets of initial conditions assuming both frozen and equilibrium flow in the acceleration tube and the results are presented in table 4. The table shows that the initial conditions used for the computations should result in lower values of shock speed and post-shock pressure. The expected difference due to the initial conditions is approximately 6 percent.

The Mach 17 case is characterized by a low acceleration tube fill pressure and an acceleration tube shock speed of over 5 km/sec. This combination of a strong shock and low density leads to significant nonequilibrium behind the shock. To help separate the influence of finite-rate chemistry from viscous effects, an inviscid simulation with finite-rate chemistry is presented first. Figure 5 is a plot of the shock and interface speed versus distance from the diaphragm. It is seen that the shock speed decreases significantly as it travels down the tube while the interface speed increases slightly. To help understand this phenomenon, the predicted speeds for the shock and interface from table 4 assuming both equilibrium and frozen flow are also plotted. A short time after the diaphragm rupture, very little reaction has occurred in the finite-rate chemistry solution and so the speed is most closely approximated by the frozen solution. At later time, as the nitrogen dissociates, the shock speed adjusts toward the equilibrium solution. To further illustrate this, figure 6 shows plots of pressure and temperature versus time at a location near the end of the acceleration tube. The interpretation of this plot is aided by recalling the x-t diagram in figure 1. The feature which arrives first at the end of the tube is the acceleration tube shock followed by the interface separating the acceleration gas and test gas. The interface signals the start of the test time. The test time ends when the secondary rarefaction arrives causing a rise in pressure. The finite-rate dissociation of the nitrogen behind the secondary shock is clearly identified from the nonuniform temperature. The temperature drops from 12,000 K just behind the shock to approximately 6000 K at the interface. In equilibrium or frozen flow, the post shock temperature would be a constant value.

Simulations with a laminar boundary layer and finite-rate chemistry were performed for the Mach 17 condition with several different grids. All of the solutions used a  $400 \times 63$  grid (63 points normal to the wall) and the grid spacing at the wall was varied to assess whether adequate resolution was placed in the boundary layer. One measure of how well the boundary layer is resolved on each grid is

to monitor the time varying distance between the shock and the interface as these features travel down the acceleration tube. This separation distance,  $l$ , can vary greatly from the value predicted by 1-D theory due to the influence of the boundary layer produced behind the shock. According to Mirels' analysis, the separation distance is expected to approach a limiting value,  $l_m$ , when the mass flow passing through the secondary shock equals the mass being entrained into the boundary layer. A plot of the separation distance versus time after diaphragm rupture for the various grids is shown in figure 7. The grid spacing at the wall was set initially set to 100  $\mu\text{m}$  and successively refined in four different simulations. The results show that a near constant limiting value of  $l_m$  is established relatively quickly after the diaphragm rupture and that the computed value of  $l_m$  decreases with decreasing grid spacing. There is approximately 6.7 percent change in  $l_m$  between the two finest grids. The value of  $l_m$  on the finest grid is 0.103 m which compares to a separation distance of approximately 1.2 m at the end of the acceleration tube for the inviscid solution. Values of pressure and temperature in the test gas at the end of the acceleration tube change by less than 1 percent between the finest grids. No further grid refinement was done because of cost. The solution on the finest grid required approximately 700,000 iterations and 70 hours of single processor central processing unit (CPU) time on a Cray C90. The difficulty in achieving a grid independent solution can be traced to the combination of a high post-shock temperature and a cold wall. This creates an extremely small thermal boundary layer which is difficult to resolve. As a further check of the solution, the value of  $l_m$  predicted by Mirels' analysis (see Mirels, 1963) is calculated to be approximately 0.098 m and is also given in figure 7. The close agreement between the computation and theory is reassuring although exact agreement is not expected because Mirels' assumption of equilibrium behind the shock is not valid for this case. A final point about grid resolution: since the state of the gas upstream of the interface is quite different from state of the gas downstream of the interface, it is possible to resolve adequately the boundary layer in one region but not the other. For the Mach 17 initial conditions and a laminar boundary layer, it appears that the region between the shock and interface is the most challenging to resolve. Therefore, adequate resolution in this region implies adequate resolution in the test-gas region.

Figure 8 depicts the computed shock and interface speed obtained from the finest grid solution with laminar flow along with the speeds from the inviscid simulation presented earlier. As predicted by Mirels' analysis, the shock and interface speeds approach the same value as the limiting flow condition is reached. Significant attenuation of

the shock speed is observed with the final value of 5110 m/sec being 9.6 percent below the inviscid, equilibrium value (see table 4). A difference between the present simulations and Mirels' analysis is the slow decrease of the shock and interface speed after the limiting flow condition is reached. Mirels' formulation predicts that the speeds reach a steady limiting value because shock attenuation due to viscous forces is assumed to be negligible, whereas the simulations include this effect. Added to figure 8 are experimentally measured shock speeds in the acceleration tube from two shots. These shock speeds are higher than the computed values for viscous flow as is expected from the different initial conditions. The overall variation in the shock speed is similar to the computations, with the highest rate of attenuation occurring closer to the diaphragm. The cause of the slight rise in the experimental shock speed at 10 m along the acceleration tube is not known.

Figure 9 shows a comparison of the pressure and temperature traces at the end of the acceleration tube for the simulations with inviscid and laminar flow. The time axis for the laminar simulation has been adjusted so that the time of arrival of the interface is the same for each case. The viscous solution has a lower post-shock pressure and temperature due to the reduced shock speed and a much smaller distance between the shock and interface as discussed above. There is also some variation in the pressure during the test time in the viscous solution. However, if this nonuniformity is judged acceptable then the test time for the laminar boundary layer solution is similar to the test time predicted by the inviscid simulation.

A comparison of an experimental and computed pressure trace at the end of the acceleration tube is presented in figure 10. There is good agreement between the pressure traces, specifically the post-shock pressure level and the variation of pressure during the test time. The opposite axis of the figure shows the value of the displacement thickness at the exit of the tube. The height of this axis is set equal to the radius of the acceleration tube to allow an easy comparison of the displacement thickness to the radius of the tube. The displacement thickness is computed using the formula for axisymmetric flow

$$\rho_{CL} u_{CL} \int_0^{R-\delta^*} 2\pi r dr = \int_0^R \rho u 2\pi r dr \quad (1)$$

where  $\delta^*$  is the displacement thickness,  $R$  is the radius of the tube, and the subscript  $CL$  refers to the centerline values. The sharp peak in the displacement thickness at the interface results from the integration path crossing the curved interface. The plot reveals that the minimum pressure during the test time is associated with a maximum in the displacement thickness. The location of the maximum

displacement thickness also corresponds to a maximum in velocity and a minimum in density and temperature (see figs. 11 and 12). This variation of flow properties is similar to the variation expected for a steady subsonic flow in a converging-diverging channel. Figure 11 shows the acceleration of the gas from 4600 m/sec just behind the shock to approximately 5150 m/sec at the interface. Since the limiting flow condition has been reached, the flow must accelerate so that the velocity at the interface is equal to the shock speed. The increase in displacement thickness after the interface causes a further velocity increase to over 5300 m/sec, which is higher than the shock speed. The predicted test gas temperature shown in figure 12 is less than 1000 K. This is significantly lower than the value of 1223 K which was computed from experimental measurements (see table 2).

Figure 13 shows the experimental and computed values of the ratio of pitot pressure to static pressure at the acceleration tube exit, averaged over the test time. The computed pitot pressure is defined as  $0.92 \rho u^2$ , an approximation based on the hypersonic limit of an ideal gas with no vibrational energy, which results in an error of at most a few percent. The predicted values of pitot pressure are higher than the experimental values and the computed the boundary layer is thinner. A comparison between the centerline pitot pressure traces is shown in figure 14. The secondary interface is identified by the sudden rise in pitot pressure shortly after the arrival of the acceleration tube shock. There is good agreement between the measured and computed values of the shock and interface separation distance but the computed value of the pitot pressure during the test time is significantly overpredicted.

Plots showing the grid, density contours, and velocity contours at an instant in time when the shock is near the end of the acceleration tube are presented in figure 15. The grid shows the clustering of points at the wall, the shock, and the interface. The density contours show the interface which is curved near the wall, giving an indication of the gas being entrained into the boundary layer. The boundary layer growth is also seen in the density contours. The velocity contours show the acceleration of the gas between the shock and interface which results in an interface speed equal to the shock speed. It is also seen that a large core flow is available for test purposes.

The source of the differences between the computationally predicted and experimentally reported values of test-gas temperature and pitot pressure is not fully understood. It is the authors' opinion that better agreement should be achievable for this case with proper modeling of all the relevant physical phenomena. Several additional simulations were used to identify significant sources of disagreement. One calculation included initial conditions

which better matched the reported experimental initial conditions, and another calculation included vibrational nonequilibrium. Neither produced significantly better agreement with data. One final computation was performed to investigate the influence of the secondary diaphragm. It is known from experimental pressure traces taken near the secondary diaphragm that there is a disturbance created by the intermediate tube shock wave interacting with and partially reflecting off the diaphragm. Roberts, et al. (1994) suggest that the HYPULSE Mach 17 condition can be especially affected by the secondary diaphragm because the entire volume of test gas originates from approximately 4 cm of compressed gas upstream of the diaphragm. As a crude model of the secondary diaphragm rupture process, the secondary diaphragm was held fixed for 10  $\mu$ sec after the arrival of the incident shock wave. This produced better agreement with the pitot pressure and temperature data while only slightly modifying the predicted static pressure trace, which suggests that the secondary diaphragm rupture process may indeed be the cause of the current discrepancies.

While the pressure trace obtained with a laminar boundary layer is in good agreement with the experimental data, the comparison in the region after the arrival of the secondary rarefaction (after the test time is over) may be fortuitous. Experimental heat transfer measurements suggest that the boundary layer becomes turbulent 500-600  $\mu$ sec after the passage of the shock. A computed pressure trace from a simulation with a turbulent transition near the experimentally measured location is presented in figure 16. The grid used for this computation had a spacing of 50  $\mu$ m at the wall. It is known that this grid is inadequate to resolve the turbulent boundary layer, but the simulation is useful to demonstrate qualitatively the effect of the transition. As was done in figure 10, the computed displacement thickness is presented on the opposite axis. The turbulent boundary layer produces an increase in displacement thickness and a corresponding reduction in static pressure starting near the transition point. As a result, the computed pressure with the turbulent transition falls significantly below the experimental measurements in the region after the test time. Even though this solution differs more from the experiment, it may be more accurate. The reason for the difference may be that in the experiment, a wave created by the reflection of the head of the rarefaction off the primary interface (a phenomenon not captured in the present simulations) is arriving at the end of the tube at approximately the same time as the turbulent transition. The arrival of this wave is suggested by the appearance of larger amplitude noise in the experimental pressure traces and by the simulations of Jacobs (1992). This wave would cause a rise in pressure and would move the predicted



trace for the transitional case closer to the data. Simulations including the primary diaphragm should be performed to clarify this issue.

### Mach 14 HP HYPULSE Test Condition

As with the Mach 17 simulations, the simulations for the Mach 14 HP conditions are for experiments using nitrogen. The nominal initial conditions for the experiments and measured test gas state are listed in tables 1 and 2, respectively. A 10 m acceleration tube length is used for this condition, with a L/D value of approximately 66. The initial conditions used for the computations are found in table 3 and are seen to be essentially the same as the experimental values. Acceleration tube post-shock conditions assuming both frozen and equilibrium flow are found in table 5. Table 5 presents separate values of the acceleration tube post-shock conditions for both the experimental and the computational-initial conditions.

The acceleration tube fill pressure for the Mach 14 HP case is much higher than it is for the Mach 17 condition (193 Pa versus 7.2 Pa) and the acceleration tube-shock speed is lower (approximately 4 km/sec versus 5 km/sec). As a result, this case has a significantly higher post-shock pressure and a lower post-shock temperature with less dissociation and gas much closer to chemical equilibrium. Consequently, there is less difference between the frozen and equilibrium solutions for this case. This is shown in figure 17 in plots of frozen and equilibrium shock speed and interface speed versus distance from the diaphragm. Also added to the plot is an inviscid, finite-rate chemistry solution. As before, the shock and interface for the inviscid finite-rate solution initially move at speeds closer to the frozen values and approach the equilibrium values at later times.

It is known from the experimental data that the boundary layer in the region between the shock and interface is laminar, and transition to turbulence occurs at the start of the test time just behind the interface. For this reason, the simulations specify a turbulent boundary layer starting 2.54 cm behind the interface. A  $450 \times 53$  grid was used and solution accuracy was studied by varying the grid spacing at the wall. An acceleration tube with half the length (5 m instead of 10 m) was used in order to minimize computer time requirements for the grid refinement study. Figure 18 shows the computed distance between the shock and interface versus time after diaphragm rupture for several simulations. Solutions with 25  $\mu\text{m}$  and 12.5  $\mu\text{m}$  grid spacing at the wall yield nearly identical results, indicating that the 25  $\mu\text{m}$  grid is adequate for resolving the region between the shock and interface. This region is more easily resolved for this case than for the

Mach 17 case because the maximum gradient associated with the thermal boundary layer is smaller. The figure also shows that the flow is far from achieving the limiting flow condition (i.e., the shock and interface are not traveling at the same speed) with the separation distance at the end of the 5 m acceleration tube being not too different from the inviscid solution. Added to figure 18 is a plot of the distance between the shock and interface for a simulation without a turbulent transition (i.e., a fully laminar boundary layer) on the 12.5  $\mu\text{m}$  grid. This solution is very similar to the other solutions showing that the transition to turbulence behind the interface has little effect on the time evolution of the flow between the shock and interface. Therefore Mirels' analysis for a laminar boundary layer is applicable. Assuming a shock speed of 3900 m/sec at the limiting flow condition, Mirels' analysis predicts  $l_m$  to be approximately 3.1 m. Using this value of  $l_m$ , the separation distance at 5 m from the diaphragm is predicted to be 0.48 m, which is in good agreement with the numerical simulation.

While the flow between the shock and interface is well resolved using the grid with 25  $\mu\text{m}$  spacing at the wall, the turbulent boundary layer behind the interface requires a finer grid. This can be seen in plots of static pressure and displacement thickness at the exit of the acceleration tube in figure 19 (the time axis for the 25  $\mu\text{m}$  grid spacing was moved slightly to align the interfaces). As mentioned previously, the peak in the displacement thickness near the interface is a numerical artifact caused by the integration path crossing the curved interface. The figure shows that the solutions using grids with 25  $\mu\text{m}$  and 12.5  $\mu\text{m}$  spacing at the wall are only slightly different in the region between the shock and interface but are significantly different at later times. The grid with the smaller spacing at the wall results in a larger boundary layer. This affects the values at the tube centerline at later times, causing the static pressure to be overpredicted on the coarser grid.

The solution for the full 10 m length acceleration tube is computed using a grid spacing of 25  $\mu\text{m}$  at the wall (the 12.5  $\mu\text{m}$  grid spacing was judged to be too expensive). It is known from the grid resolution study that this grid will accurately capture the time evolution of the shock and interface but it will underpredict the boundary layer thickness in the test gas. The variation of the shock and interface speed in the acceleration tube for the viscous simulation are found in figure 20, along with the inviscid computation presented earlier. The effect of the boundary layer is to cause a deceleration of both the shock and the interface. At the end of the acceleration tube, the speed difference between the shock and interface is still large indicating that the limiting flow conditions have not been reached. Also shown in figure 20 are experimental shock

speeds which are slightly lower than the computed values but show a similar rate of shock attenuation.

The time history of the separation distance between the shock and interface for the 10 m acceleration tube, shown in figure 21, indicates a separation distance of approximately 0.8 meters at the end of the tube. Mirels' formula for the separation distance 10 m from the diaphragm gives a value of 0.84 m. Pressure and temperature traces for the inviscid and turbulent case are plotted in figure 22 (the time axis of the inviscid solution has been translated slightly to align the interfaces). As with the Mach 17 case, the post-shock pressure is lower for the viscous solution than for the inviscid solution because of shock attenuation. The pressure history for the viscous solution differs significantly from the inviscid solution most notably by a large and monotonic increase in pressure during the test time.

A comparison of the experimental and computed pressure traces at the end of the acceleration tube is presented in figure 23. Both the experiment and simulation show similar characteristics and are in good agreement. There is a drop in pressure around the transition point and a steady rise in pressure over the test time. The opposite axis of the figure shows the value of the displacement thickness at the exit of the tube. This axis is scaled to the tube diameter. As with the Mach 17 simulation, the minimum pressure over the test time is associated with a maximum in the displacement thickness. The drop in pressure at the start of the test time is seen to be associated with the sudden rise in the displacement thickness at the transition point. The subsequent decrease in the displacement thickness seems to be the cause of the rise in pressure during the test time; however, it is difficult to distinguish between this effect and the arrival of the rarefaction. Figure 23 also illustrates that the variation of pressure during the test time makes it difficult to precisely determine the beginning and end of the test time. Time histories of density, velocity, and temperature are presented in figures 24 and 25. During the test time, these quantities vary approximately linearly with time. The computed values in the plot can be compared with the experimental values presented in table 2, which are averaged over the test time. Of particular note in figure 24 is the coincidence of the turbulent transition point with a large and sudden increase in the velocity.

A comparison of experimental and computed pitot pressures at the tube exit is shown in figure 26. As before, the computed pitot pressure was averaged over the test time and defined as  $0.92 \rho u^2$ . Both the experiment and solution show very little or no core flow and the agreement can be described as fair. From the grid study discussed above, it is known that a finer grid would yield a thicker boundary

layer. In addition, there are several parameters in the turbulence model, such as the intermittency factor, which can significantly affect the solution. This is another possible cause of the difference between the computation and the experiment. A comparison between the experimental and predicted time-varying pitot pressures is presented in figure 27. Figure 27(a) presents the comparison at the centerline and figure 27(b) presents the comparison 1.27 cm above the tube wall. Both figures reveal that the distance between the shock and interface is accurately predicted by the simulation. The pitot trace 1.27 cm above the wall shows an overshoot just after the interface arrival. The overshoot is interpreted to be the test-gas pitot pressure ahead of the turbulent transition. After transition, the boundary layer thickens rapidly causing a sudden drop in pitot pressure. The shorter duration overshoot in the computation suggests that the transition point (2.54 cm behind the interface) may have been specified too close to the interface. A transition a few more centimeters behind the interface would likely increase the width of the overshoot and give better agreement with the data. This hypothesis is supported by the location of the drop in measured static pressure associated with transition in figure 23. The drop appears to occur at a later time than in the computation, indicating that a specified turbulent transition farther from the interface would probably give better agreement with the data.

Plots showing the grid, density contours, and velocity contours at an instant in time when the shock is near the end of the acceleration tube are presented in figure 28. The density contours show the large growth in the boundary layer associated with the turbulent transition. This results in a small core flow with minimum diameter near the interface and larger diameter farther behind the interface.

To show the rate of growth of the boundary layer as the shock travels down the acceleration tube, the pressure and displacement thickness traces for the 5 m and 10 m acceleration tubes are plotted together in figure 29. Both solutions used a grid spacing of  $25 \mu\text{m}$  at the wall and the time of arrival of the interfaces have been aligned in the figure. The post-shock pressure is higher for the trace at 5 m than it is at 10 m because the shock has not attenuated as much at 5 m. The maximum displacement thickness is computed to be 72 percent larger at 10 m than it is at 5 m. Figure 30 shows computed pitot pressure profiles at 5 m and 10 m averaged over several hundred microseconds. Although the pressure of the core flow varies with time at 5 m, this figure shows that at 5 m, approximately half the diameter of the tube is occupied by the inviscid core. This is in contrast to the profile at 10 m which shows little, if any, core flow.

It is expected that experiments in an expansion tube with higher pressures and a larger scale would result in the movement of the turbulent transition to the region between the shock and interface. Therefore, an additional simulation of the Mach 14 HP case was performed with the transition location placed just behind the secondary shock so that whole the boundary layer was turbulent. This simulation used a grid spacing of  $25\text{ }\mu\text{m}$  spacing at the wall. The results of this simulation provide some qualitative insight into the sensitivity of the test conditions to the transition location. The time evolution of the distance between the shock and interface for this case is found in figure 31 along with the case having turbulent transition at the interface. As expected, the fully turbulent boundary layer reduces the separation between the shock and interface because the boundary layer is thicker, and the separation distance with the fully turbulent boundary layer is smaller than the value predicted by Mirels' correlation for laminar flow. Figure 32 presents the variation of the shock and interface speeds for the fully turbulent case compared to the baseline case, revealing that the fully turbulent case more closely approaches the limiting flow conditions at the end of the acceleration tube. Figure 33 presents a comparison of the two cases showing static pressure and displacement thickness at the end of the acceleration tube (the arrival time of the interfaces has been aligned). Compared to the case having transition at the interface, the fully turbulent case has a larger displacement thickness and a smoother pressure trace near the interface. The computed density and velocity histories are presented in figure 34. The interface speed is greater for the fully turbulent case even though there is more shock attenuation. The velocity of the test gas is therefore slightly larger in the fully turbulent case. Overall, the differences in the test conditions which result from changing the location of turbulent transition are not large.

### **Pressure Scaling for the Mach 14 HP HYPULSE Test Condition**

The test conditions obtained for the Mach 14 HP case are less than desirable because of the large pressure rise during the test time and the small diameter of core flow. One hope to improve this situation is to raise the operating pressure within the expansion tube, thereby increasing the Reynolds number. Assuming the boundary layer in the test gas is turbulent, an increase in Reynolds number will result in a thinner boundary layer. A numerical study of the effect of pressure on boundary layer thickness requires that the boundary layers are well resolved so that differences due to changing Reynolds number are not confused with changing numerical error. Numerical simulations which investigate the effect of increasing the pressures

inside HYPULSE are not practical using the present numerical formulation because the turbulent boundary layers are already difficult to resolve and, as the Reynolds number increases, the minimum spacing at the wall must be decreased to maintain accuracy. Therefore, several simulations were made by decreasing the fill pressures from the current Mach 14 HP operating condition. Since the grid with  $12.5\text{ }\mu\text{m}$  spacing at the wall is nearly adequate at the Mach 14 HP conditions, solutions at lower pressures should be accurate using this grid and even coarser grids. The study was performed using a 5 m acceleration tube to provide an exit flow with a well defined boundary layer edge (recall that the exit flow for the Mach 14 HP condition is nearly fully developed flow making changes in boundary layer thickness difficult to discern).

Two cases were examined to study the effect of pressure on boundary layer thickness: the first case was computed with driven and acceleration-tube pressures reduced by a factor of four from the HYPULSE Mach 14 HP conditions, and the second case was computed using driven and acceleration-tube pressures reduced by a factor of sixteen. For an inviscid perfect gas, a proportionally equal pressure reduction in the driven and acceleration-tube pressures would result in exactly the same test gas conditions except for a proportional reduction in the test gas pressure. This is not true when the boundary layer and nonequilibrium chemistry are included. As the pressure is reduced, boundary layer thickness is increased and the departure from chemical equilibrium is increased. For the reasons just mentioned, accounting for the differences between the scaled pressure cases is not straightforward. Nevertheless, the present study illustrates how pressure changes can affect boundary layer growth. To help constrain the differences between the cases, the turbulent transition point was kept fixed at a location just behind the interface even though in a real experiment it is expected that the transition would occur at different locations with changing Reynolds number. The case with the factor of four pressure reduction was computed with  $12.5\text{ }\mu\text{m}$  grid spacing at the wall while the case with the factor of 16 pressure reduction was computed with  $25\text{ }\mu\text{m}$  spacing.

Figure 35 presents a plot of the separation distance between the shock and the interface for the scaled pressure cases and an additional computation with a laminar boundary layer using the Mach 14 HP fill pressures. The plot shows that lowering the pressure decreases the separation distance and causes the flow to be closer to the limiting flow conditions at the end of the acceleration tube. The case with the pressure reduced by a factor of 16 very nearly reaches the limiting flow condition. Figure 36 presents the computed pressure traces. In order to compare the pressure traces directly, the factor used to reduce

the fill pressures was used to re-scale the post-shock pressures. The figure shows that the re-scaled post-shock pressures become lower as the fill pressure was reduced. This is because greater shock attenuation occurs at lower Reynolds numbers. All the cases, except the laminar case, show a similar rise in pressure during the test time. Figure 37 is a plot of the displacement thickness for the various cases with labels noting the maximum values. The laminar case is included on the plot to show the much larger displacement thickness of the turbulent boundary layer.

For a turbulent boundary layer on a flat plate, the displacement thickness is expected to vary as  $\delta^*_{\infty} \propto 1/\rho^{1/5}$  (see Schlichting, 1979). The present computational results indicate that for the test gas in HYPULSE, the displacement thickness may vary with an exponent of 1/8 to 1/9 rather than 1/5. This suggests that increasing the operating pressure in an expansion tube may not provide the decrease in boundary layer thickness that one would expect from flat-plate correlations. Reasons to expect a growth rate different from flat-plate correlations include the entrainment of acceleration gas in the test gas boundary layer, the effect of the decreasing pressure through the secondary expansion, and the fact that the flow is axisymmetric.

## Conclusions

Axisymmetric simulations of both laminar and turbulent flow of nitrogen in the HYPULSE expansion tube were shown to be in good agreement with experimental data. A major finding of these simulations is that the observed test gas nonuniformity is strongly linked to the boundary layer displacement thickness. The effect of the boundary layer on the flow properties in the test gas can be qualitatively compared to subsonic flow in a converging-diverging channel. As the displacement thickness increases, higher velocities and lower pressures are observed in the core flow region. It is also shown that nonequilibrium chemistry in the shocked acceleration tube gas can have a significant effect on the shock speed.

The simulations show that the displacement thickness is larger for a turbulent boundary layer than for a laminar boundary layer in the current operating range of HYPULSE. This conclusion appears to be valid regardless of the location of the transition to turbulent flow, as long as the turbulent transition occurs prior to the arrival of most of the test gas. The large displacement thickness associated with a turbulent boundary layer causes significant variation in the core flow during the test time. This variation makes it difficult to identify the arrival of the secondary rarefaction which signals the end of the test

time. Furthermore, the rapid growth of the turbulent boundary layer limits the length of the acceleration tube for which a reasonable inviscid core can be maintained. Simulations with reduced fill pressures suggest that the boundary layer thickness in an expansion tube can be affected by changing the operating pressure, but that the dependence of the boundary layer thickness on the pressure is weaker than what is predicted by flat plate correlations.

While the simulations presented here are believed to capture accurately many of the first order boundary layer effects, several important physical processes have been neglected and should be investigated further. These include the opening of the main diaphragm, thermochemical nonequilibrium of air rather than nitrogen, and secondary diaphragm rupture mechanics. The present results suggest that the inclusion of the secondary diaphragm rupture process is particularly important in cases such as the Mach 17 condition where all of the test gas originates from a region close to the secondary diaphragm. Grid refinement studies have shown the present solutions are not grid independent and that better resolution is desirable. This demonstrates the need for more efficient computational methods such as a fully implicit, time accurate formulation and higher-order accuracy to improve the resolution of the solutions that can be obtained with available computer resources. Although the algebraic turbulence model proved useful for predicting first order effects, there is still a need for improved turbulence models.

## References

- Baldwin, B. S.; and Lomax, H.: Thin Layer Approximation and Algebraic Model for Separated Turbulent Flows. AIAA Paper 78-0257, AIAA 16th Aerospace Sciences Meeting, Huntsville, Ala., Jan. 1978.
- Cebeci, T.; and Smith, A. M. O.: Analysis of Turbulent Boundary Layers, Academic Press, New York, 1974.
- Erdos, J.; Calleja, J.; and Tamagno, J.: Increase in the Hypervelocity Test Envelope of the HYPULSE Shock-Expansion Tube. AIAA Paper 94-2524, 18th AIAA Aerospace Ground Testing Conference, Colorado Springs, Colo., June 1994.
- Gupta, R. N.; Yos, J. M.; Thompson, R. A.; Lee, K. -P.: A Review of Reaction Rates and Thermodynamic and Transport Properties for an 11-Species Air Model for Chemical and Thermal Nonequilibrium Calculations to 30,000 K. NASA RP-1232, 1990.

- Jacobs, P. A.: Numerical Simulation of Transient Hypervelocity Flow in an Expansion Tube. NASA CR-189615.
- Kamel, M. R.; Morris, C. I.; Thurber, M. C.; Wehe, S. D.; and Hanson, R. K.: New Expansion Tube Facility for the Investigation of Hypersonic Reactive Flow. AIAA Paper 95-0233, 33rd AIAA Aerospace Sciences Meeting and Exhibit, Reno, Nev., Jan. 1995.
- Mirels, H.: Test Times in Low-Pressure Shock Tubes. *Physics of Fluids*, vol. 6, no. 9, Sept. 1963, pp. 1201–1214.
- Mirels, H.: Shock Tube Test Time Limitation Due to Turbulent-Wall Boundary Layer. *AIAA J.*, vol. 2, no. 1, 1964, pp. 84–93.
- Mirels, H.: Correlation Formulas for Laminar Shock Tube Boundary Layer. *Physics of Fluids*, vol. 9, no. 7, 1966, pp. 1265–1272.
- Mirels, H.: Boundary Layer Growth in Shock Tubes. *Proceedings of the Eighth International Symposium on Shock Waves*, London, July 1971, pp. 6/1–30.
- Morgan, R. G.; and Stalker, R. J.: Double Diaphragm Driven Free Piston Expansion Tube. 18th Symposium on Shock Waves, Japan, 1991, pp. 1031–1038.
- Park, C.: Review of Chemical-Kinetic Problems of Future NASA Missions, I: Earth Entries. *AIAA J. Thermophysics and Heat Transfer*, vol. 7, no. 3, July–Sept. 1993, pp. 385–398.
- Paull, A.; and Stalker, R. J.: Test Flow Disturbances in an Expansion Tube. *J. Fluid Mech.*, vol. 245, 1992, pp. 493–521.
- Roberts, W. L.; Allen, M. G.; Howard, R. P.; Wilson, G. J.; and Trucco, R.: Measurement and Prediction of Nitric Oxide Concentration in the HYPULSE Expansion Tube. AIAA Paper 94-2644, 18th AIAA Aerospace Ground Testing Conference, Colorado Springs, Colo., June 1994.
- Schlichting, H.: *Boundary Layer Theory*, Seventh Edition. McGraw-Hill, 1979.
- Sharma, S. P.; and Wilson, G. J.: Test Times in Hypersonic Shock Tubes. AIAA Paper 95-0713, 33rd AIAA Aerospace Sciences Meeting and Exhibit, Reno, Nev., Jan. 1995.
- Shinn, J. L.; and Miller, C. G.: Experimental Perfect Gas Study of Expansion Tube Flow Characteristics. NASA TP-1317, Dec. 1978.
- Shirazi, S. A.; and Truman, C. R.: Evaluation of Algebraic Turbulence Models for PNS Predictions of Supersonic Flow Past a Sphere-Cone. *AIAA J.*, vol. 27, no. 5, May 1989, pp. 560–568.
- Srullijes, J.; Smeets, G.; and Seiler, F.: Expansion Tube Experiments for the Investigation of Ram-Accelerator-Related Combustion and Gasdynamic Problems. AIAA Paper 92-3246, 28th Joint Propulsion Conference and Exhibit, Nashville, Tenn., July 1992.
- Trimpi, R. L.: A Preliminary Theoretical Study of the Expansion Tube, A New Device for Producing High-Enthalpy Short Duration Hypersonic Gas Flows. NASA TR R-133, 1962.
- Trimpi, R. L.; and Callis, L. B.: A Perfect-Gas Analysis of the Expansion Tunnel, a Modification to the Expansion Tube. NASA TR R-223, Apr. 1965.
- Trimpi, R. L.: A Theoretical Investigation of Simulation in Expansion Tubes and Tunnels. NASA TR R-243, 1966.
- Wilson, G. J.: Time-Dependent Quasi-One-Dimensional Simulations of High Enthalpy Pulse Facilities. AIAA Paper 92-5096, AIAA Fourth International Aerospace Planes Conference, Orlando, Fla., Dec. 1992.
- Wilson, G. J.; Sharma, S. P.; and Gillespie, W. D.: Time-Dependent Simulations of Reflected Shock/Boundary Layer Interaction. AIAA Paper 93-0480, 31st AIAA Aerospace Sciences Meeting and Exhibit, Reno, Nev., Jan. 1993.
- Yee, H. C.: A Class of High-Resolution Explicit and Implicit Shock-Capturing Methods. NASA TM-101088, Feb. 1989.

Table 1. Experimental fill pressures and measured driven tube shock speeds

Condition	Driven tube shock speed (m/sec)	Driven tube fill pressure (Pa)	Acceleration tube fill pressure (Pa)
Mach 17	2800	3466	6.0
Mach 14 HP	2340	9200	193

Table 2. Experimental test gas conditions

Condition	Secondary shock velocity (m/sec)	Static pressure (Pa)	Static temperature (K)	Velocity (m/sec)
Mach 17	5253	1930	1223	5166
Mach 14 HP	3828	37,740	1455	3538

Table 3. Simulation initial conditions

Condition	Driven tube shock speed (m/sec)	Driven tube fill pressure (Pa)	Acceleration tube fill pressure (Pa)
Mach 17	2665	3466	7.2
Mach 14 HP	2355	9200	193

Table 4. Computed Mach 17 acceleration tube shock properties assuming frozen and equilibrium flow

		Experiment initial conditions	Computation initial conditions
Frozen acceleration tube gas	Shock speed (m/sec)	6401	6007
	Post-shock pressure (Pa)	2457	2595
	Post-shock temperature (K)	15,340	13,580
	Post-shock velocity (m/sec)	5588	5240
Equilibrium acceleration tube gas	Shock speed (m/sec)	6002	5654
	Post-shock pressure (Pa)	2317	2456
	Post-shock temperature (K)	5531	5443
	Post-shock velocity (m/sec)	5618	5267

Table 5. Computed Mach 14 HP acceleration tube shock properties assuming frozen and equilibrium flow

		Experiment initial conditions	Computation initial conditions
Frozen acceleration tube gas	Shock speed (m/sec)	4265	4293
	Post-shock pressure (Pa)	34,914	35,380
	Post-shock temperature (K)	7150	7273
	Post-shock velocity (m/sec)	3693	3719
Equilibrium acceleration tube gas	Shock speed (m/sec)	4156	4181
	Post-shock pressure (Pa)	34,141	34,581
	Post-shock temperature (K)	5337	5358
	Post-shock velocity (m/sec)	3706	3731

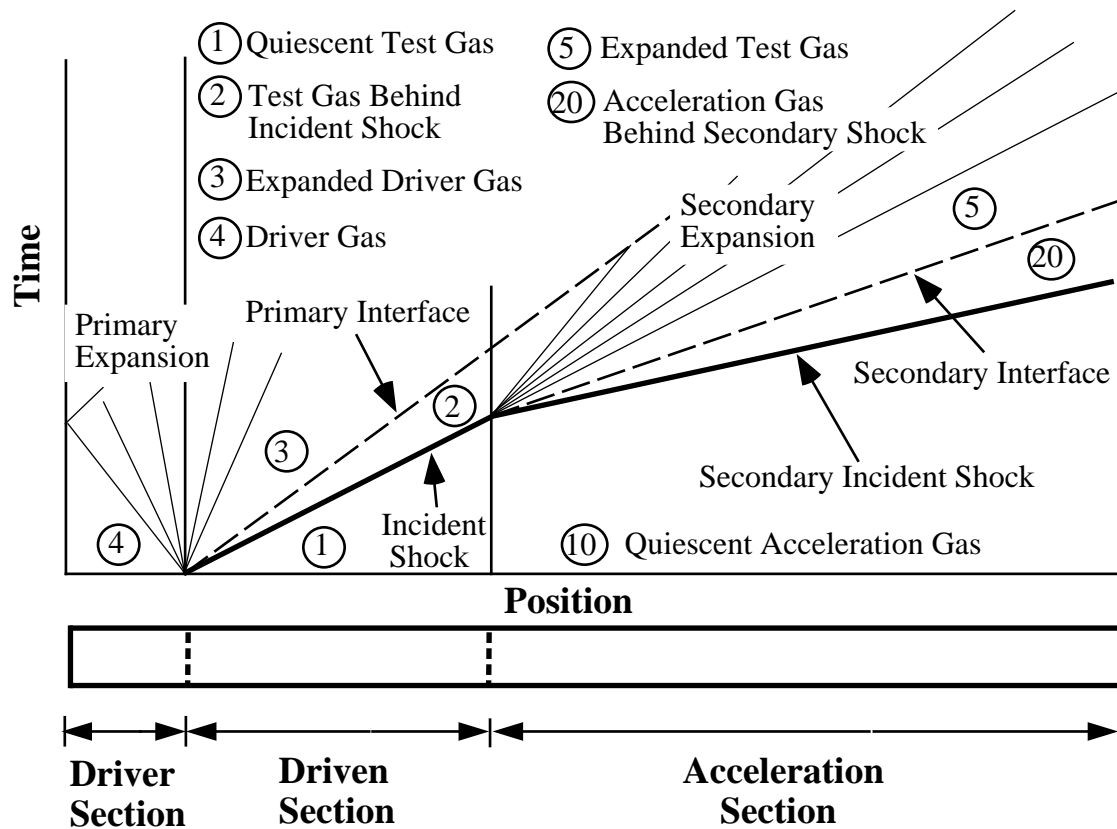


Figure 1. X-t diagram illustrating the flow within an expansion tube.



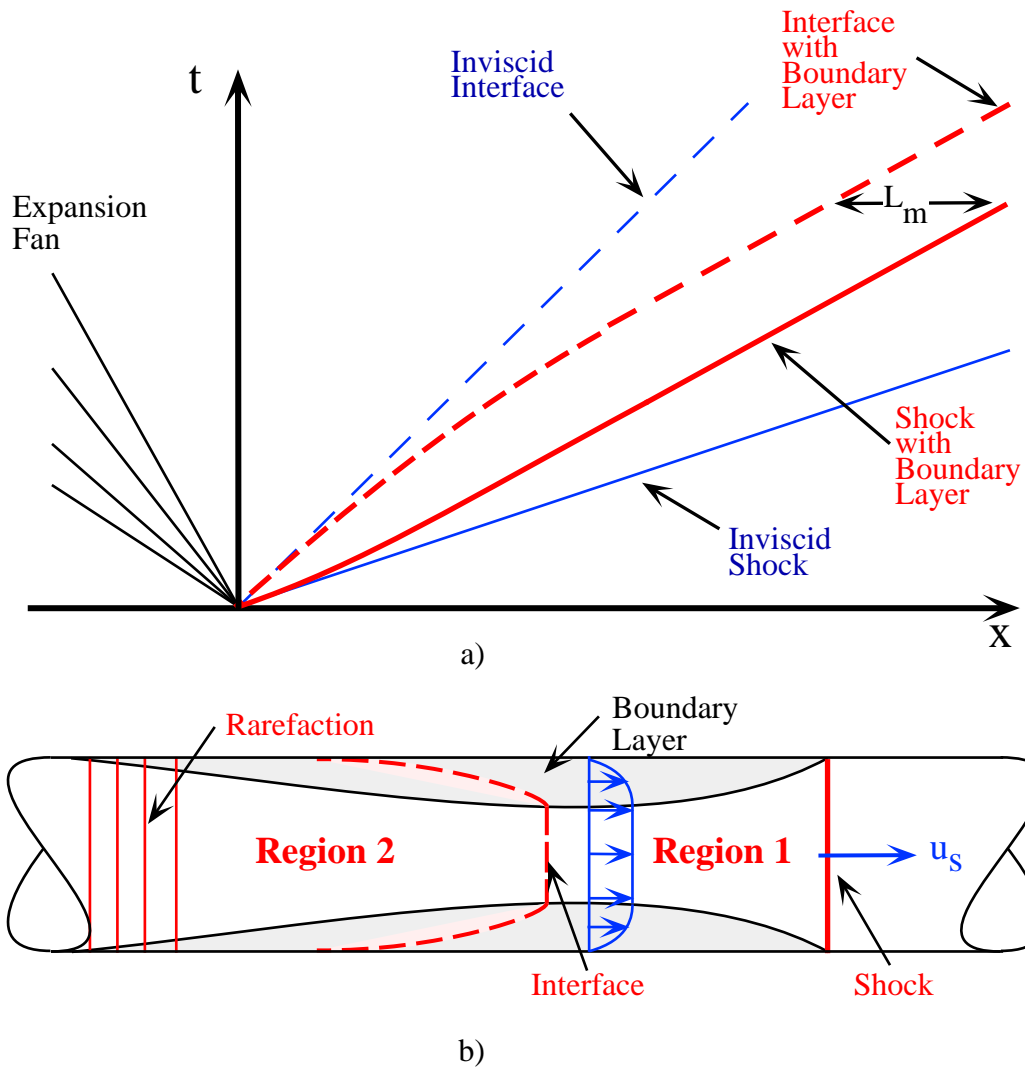
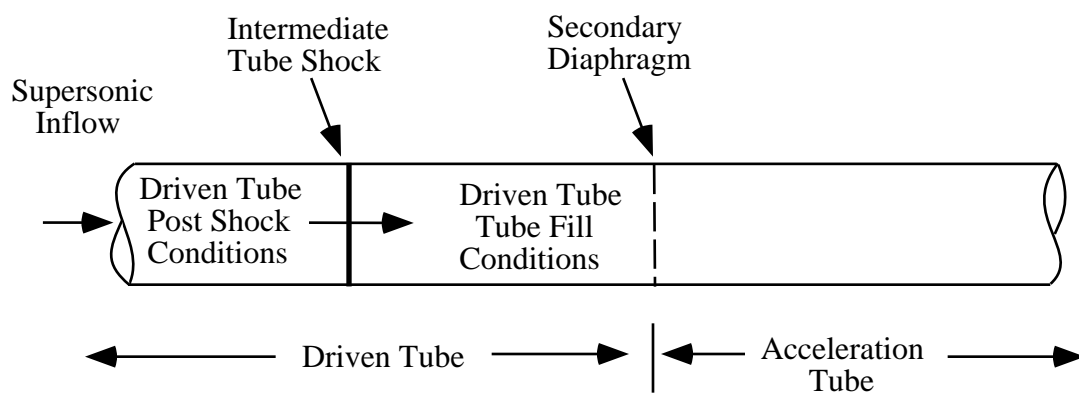


Figure 2. Influence of viscosity on shock-tube flow: a) x-t diagram, b) schematic diagram of flow features.



*Figure 3. Initial conditions for numerical simulations.*

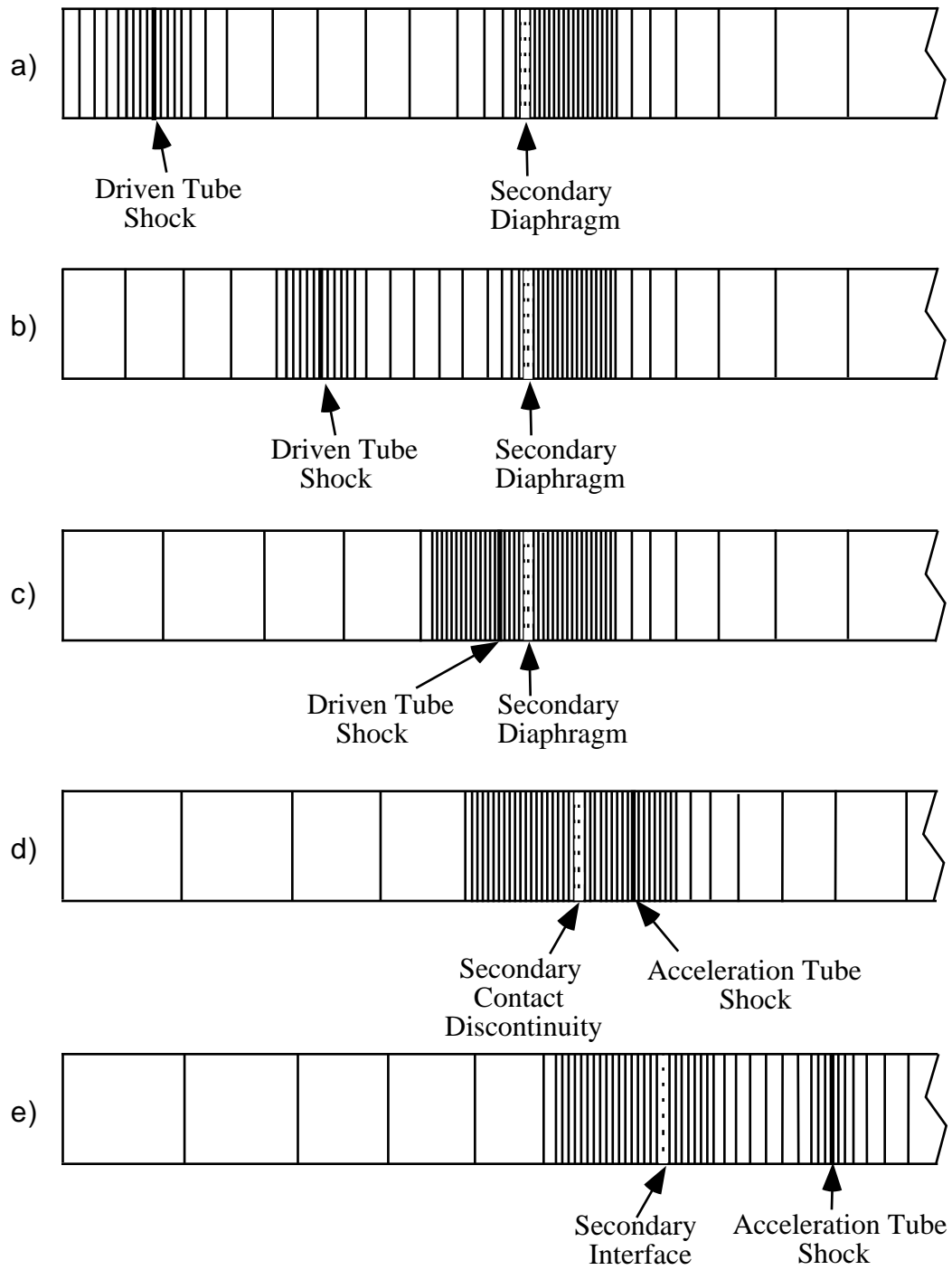


Figure 4. Schematic diagram of grid motion during simulations, showing grid clustering around shock and interface.

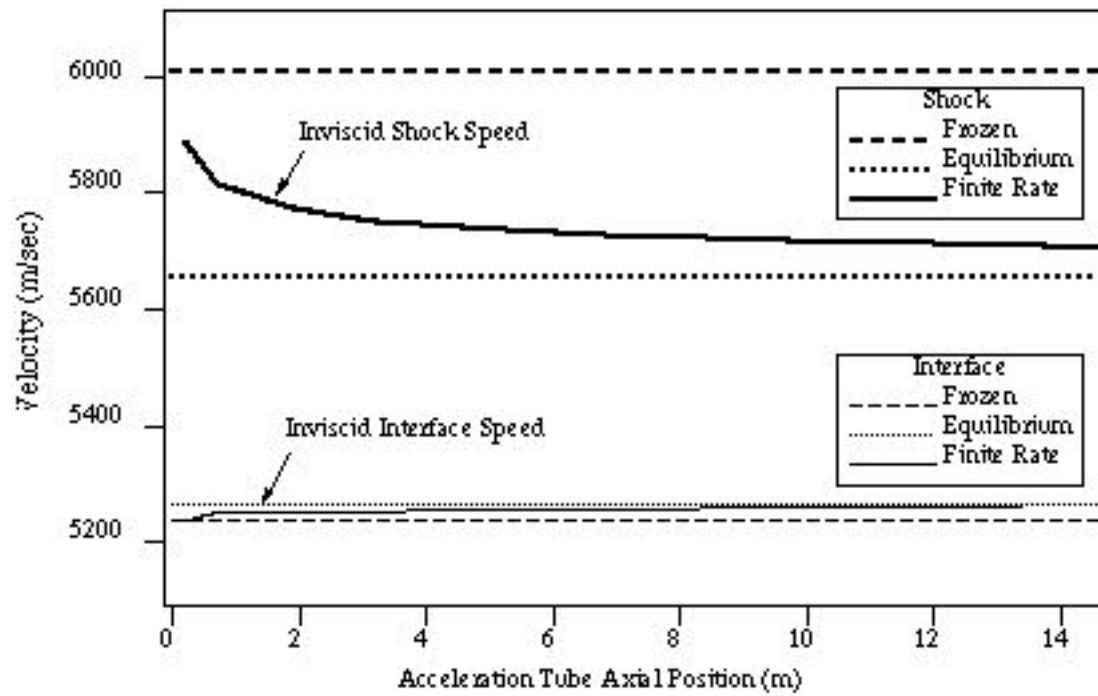


Figure 5. Computed shock speed versus distance in the acceleration tube for the inviscid simulation of the HYPULSE Mach 17 condition showing the influence of finite-rate chemistry.

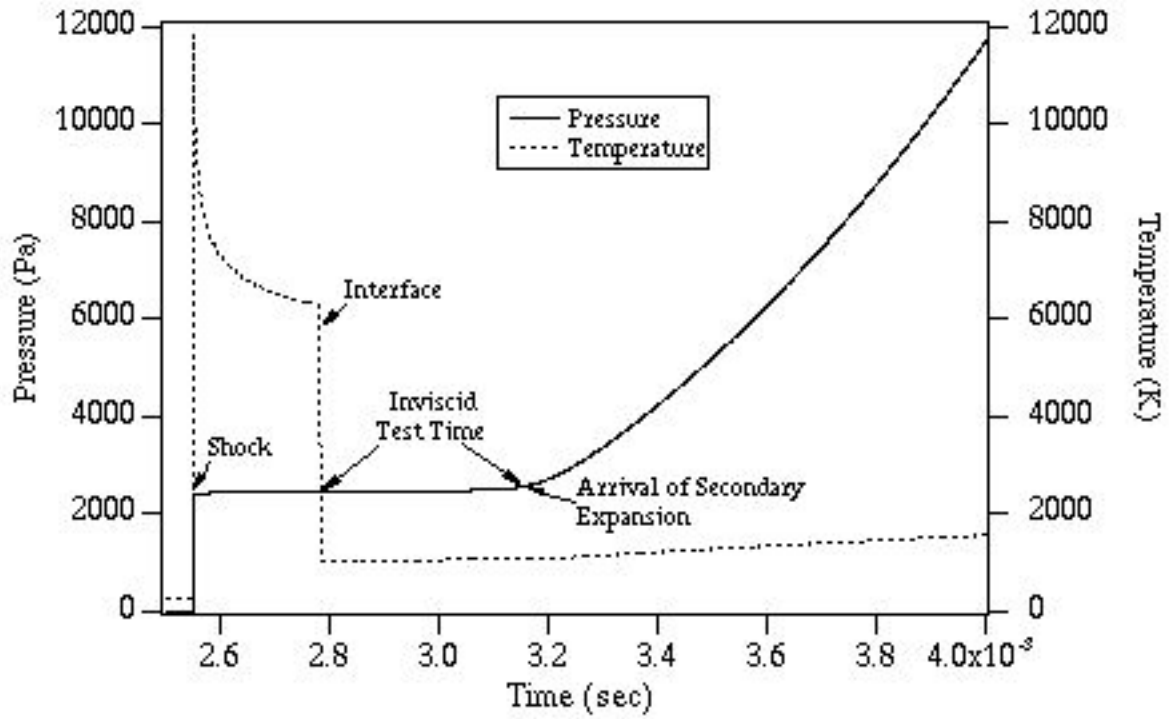


Figure 6. Computed pressure and temperature time traces at the end of the acceleration tube for the inviscid simulation of the HYPULSE Mach 17 condition.

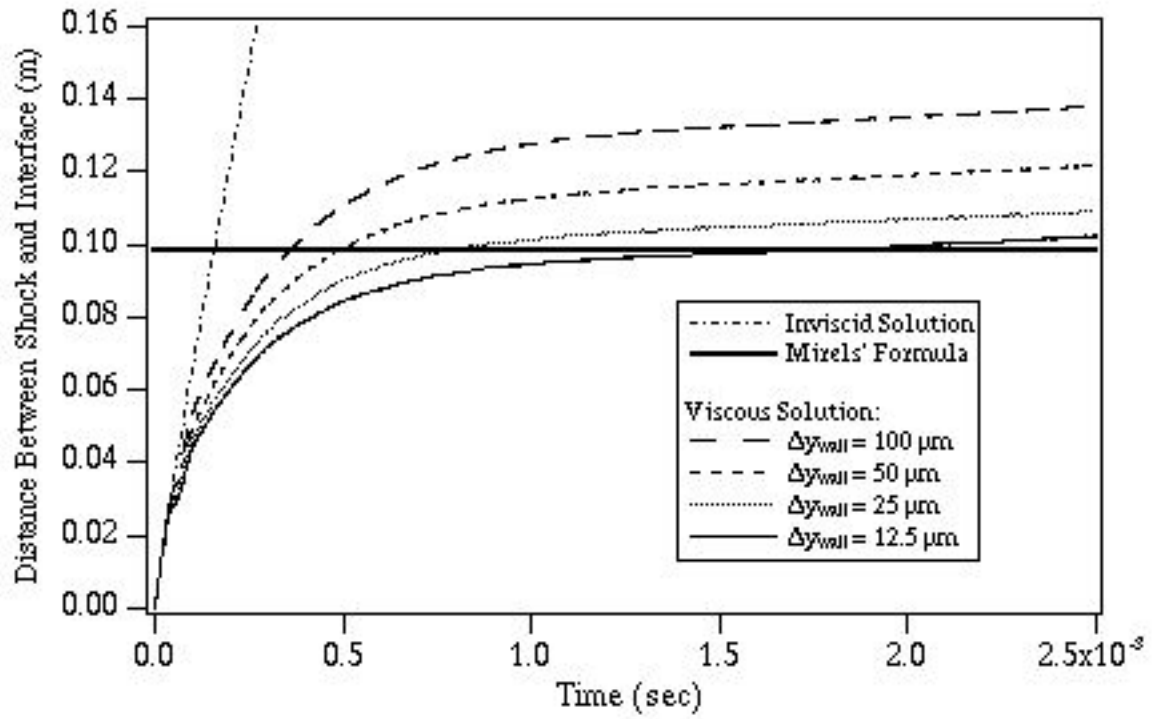


Figure 7. Computed distance between the shock and interface versus time for a grid refinement study of the HYPULSE Mach 17 condition.

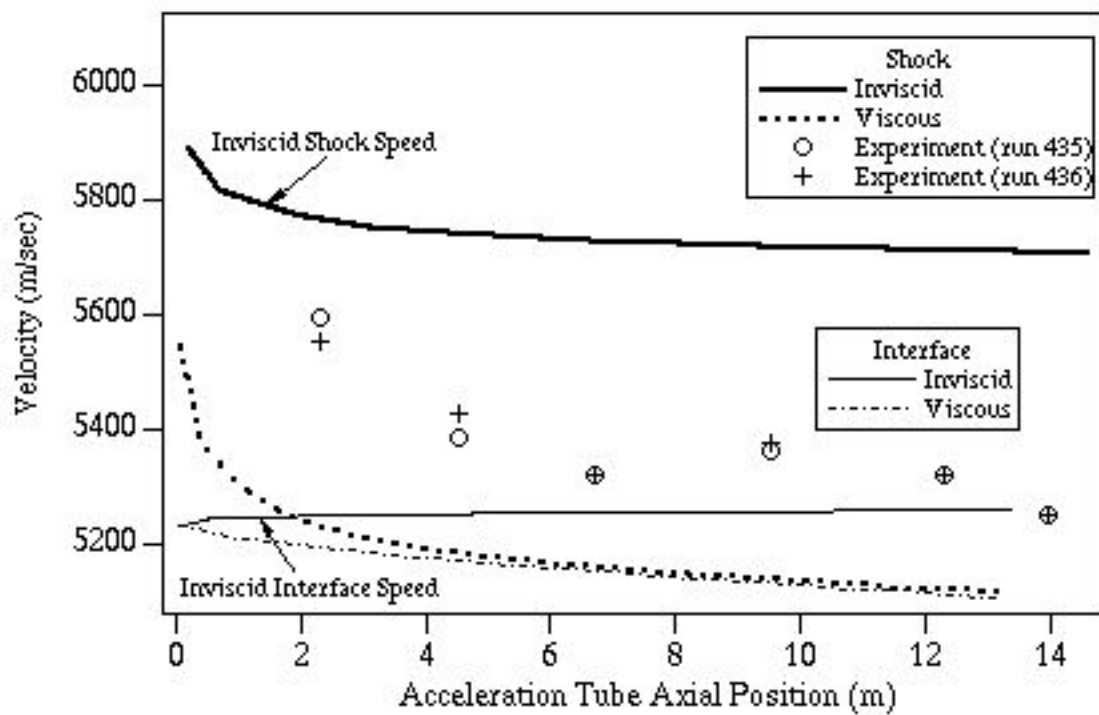


Figure 8. Computed and experimental shock speed versus distance in the acceleration tube for the HYPULSE Mach 17 condition.

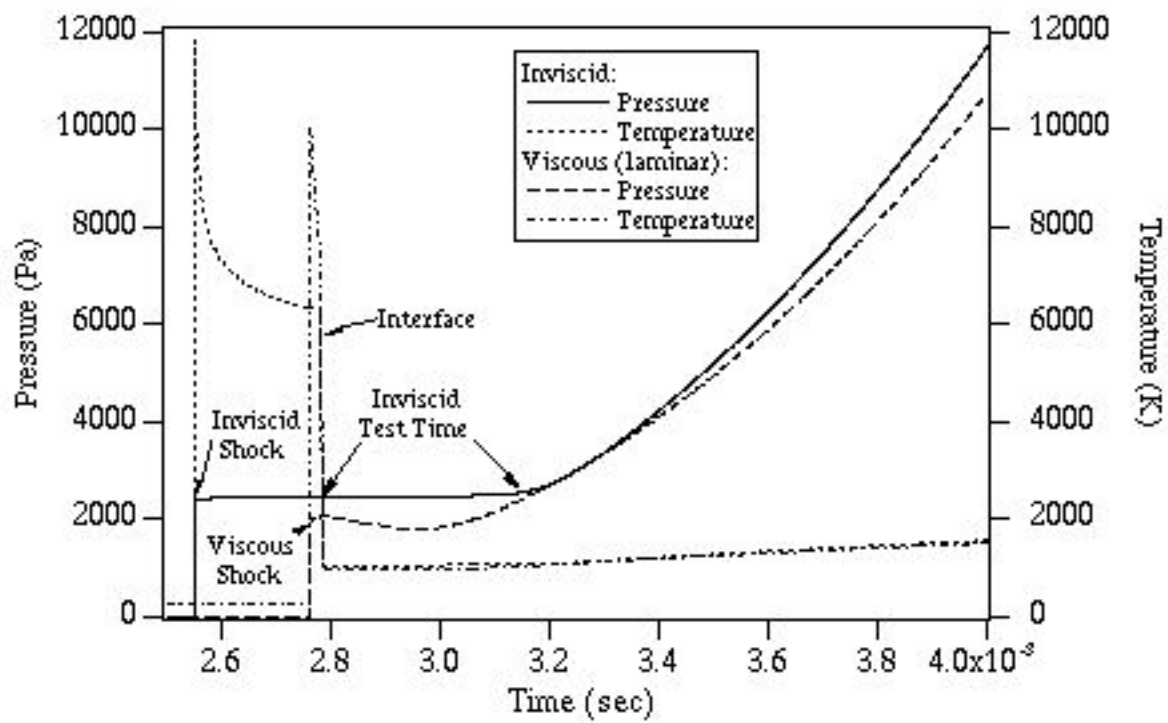


Figure 9. Computed pressure and temperature time traces at the end of the acceleration tube comparing inviscid and laminar simulations of the HYPULSE Mach 17 condition.



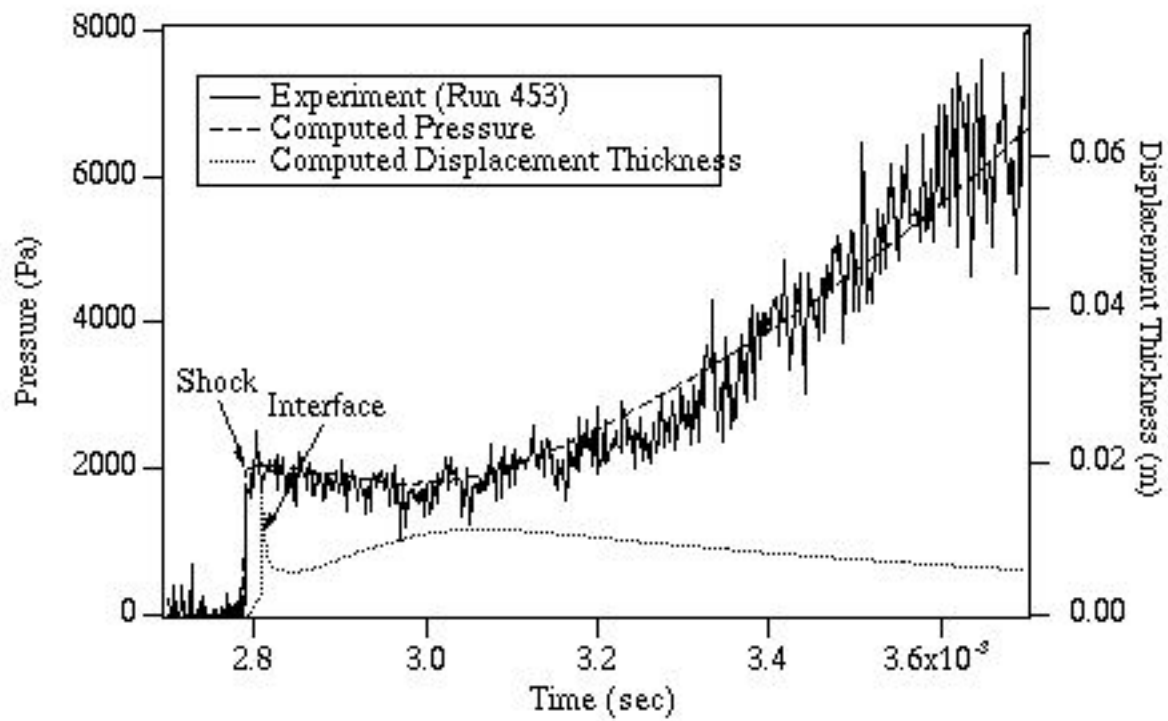


Figure 10. Computed and experimental pressure traces and computed displacement thickness at the end of the acceleration tube for the HYPULSE Mach 17 condition.

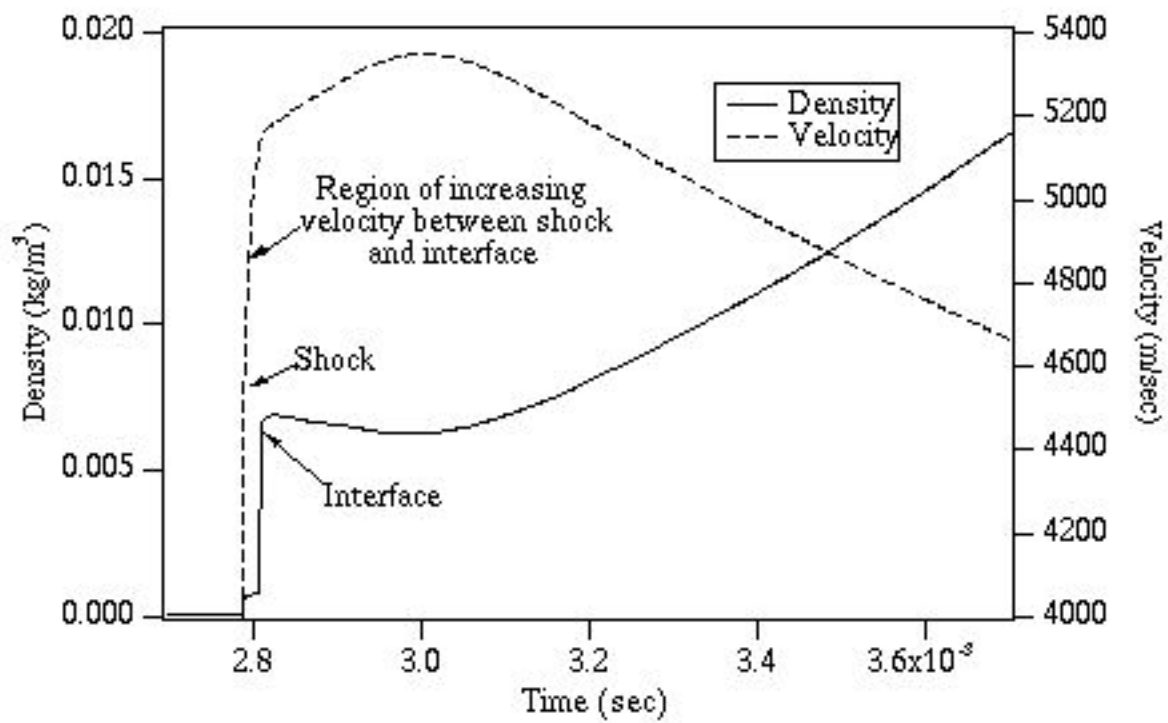


Figure 11. Computed density and velocity at the end of the acceleration tube for the HYPULSE Mach 17 condition.

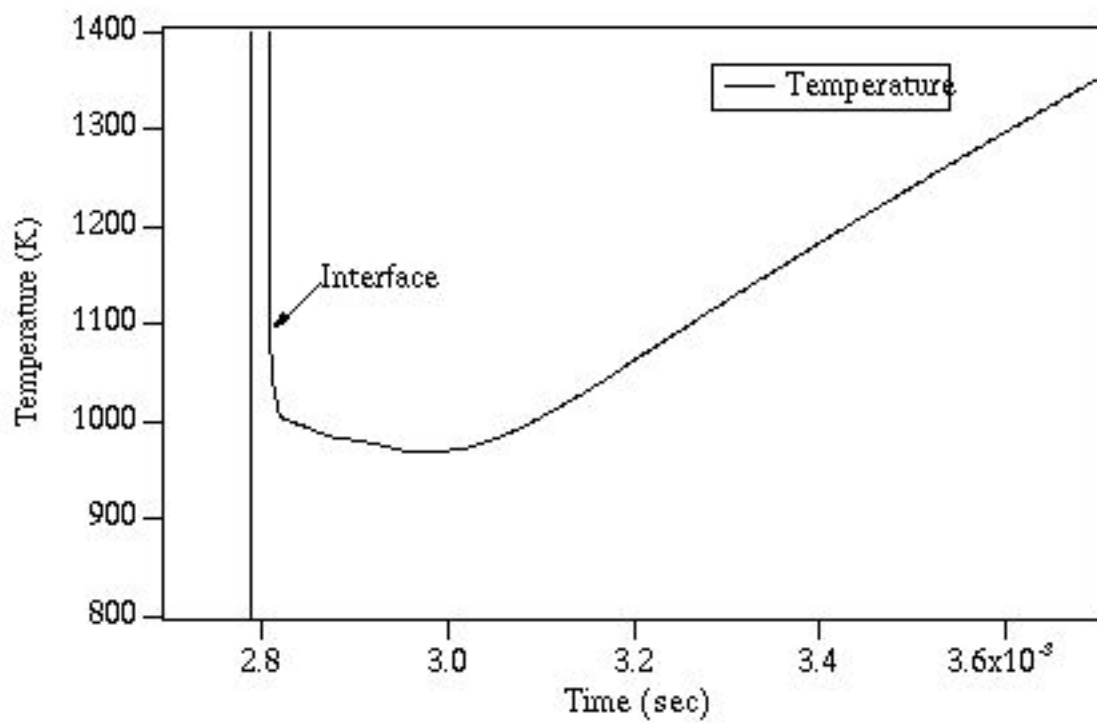


Figure 12. Computed temperature at the end of the acceleration tube for the HYPULSE Mach 17 condition.

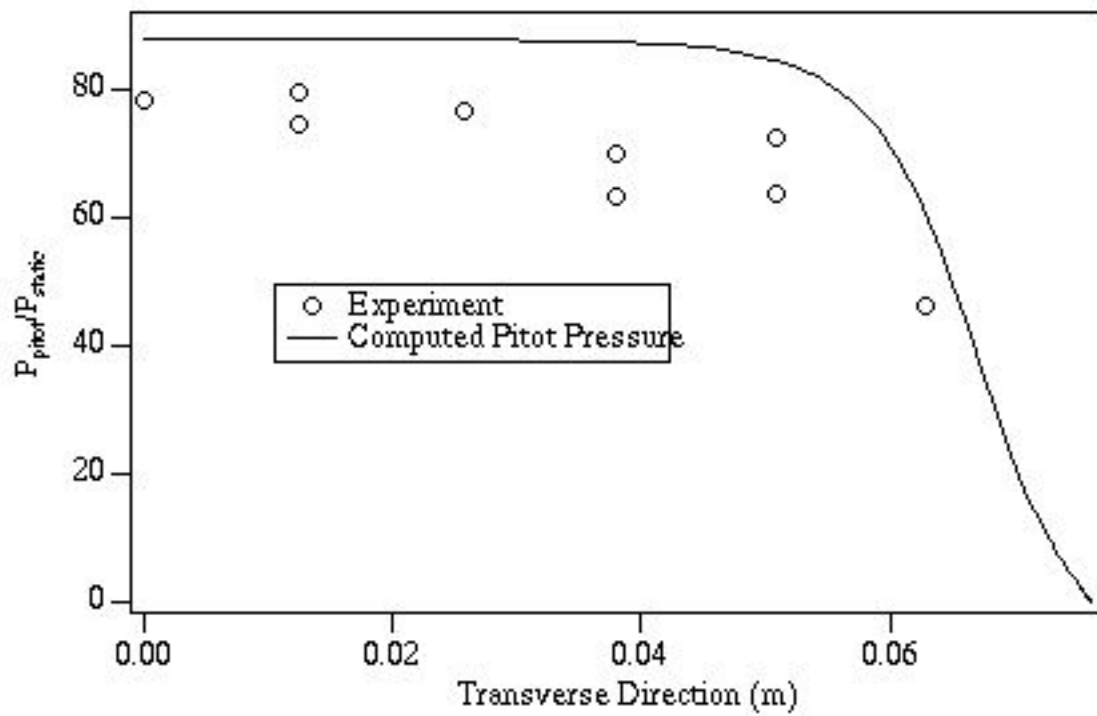


Figure 13. Computed and experimental pitot pressure profiles at the end of the acceleration tube for the HYPULSE Mach 17 condition.

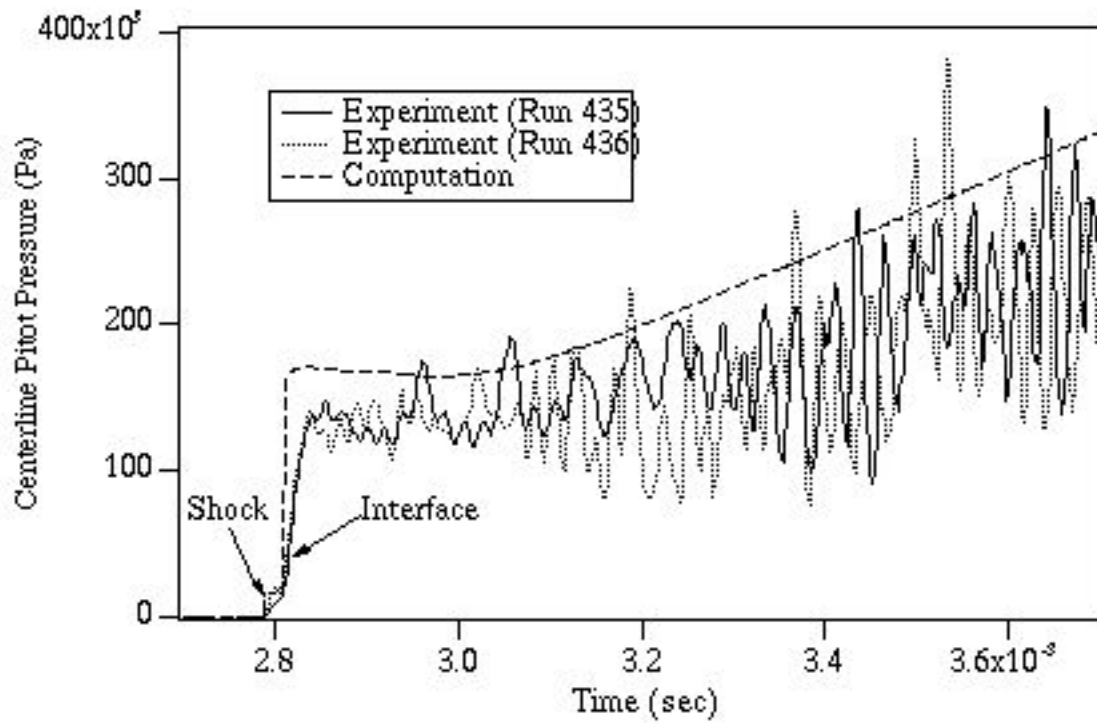


Figure 14. Computed and experimental centerline pitot pressure traces at the end of the acceleration tube for the HYPULSE Mach 17 condition.

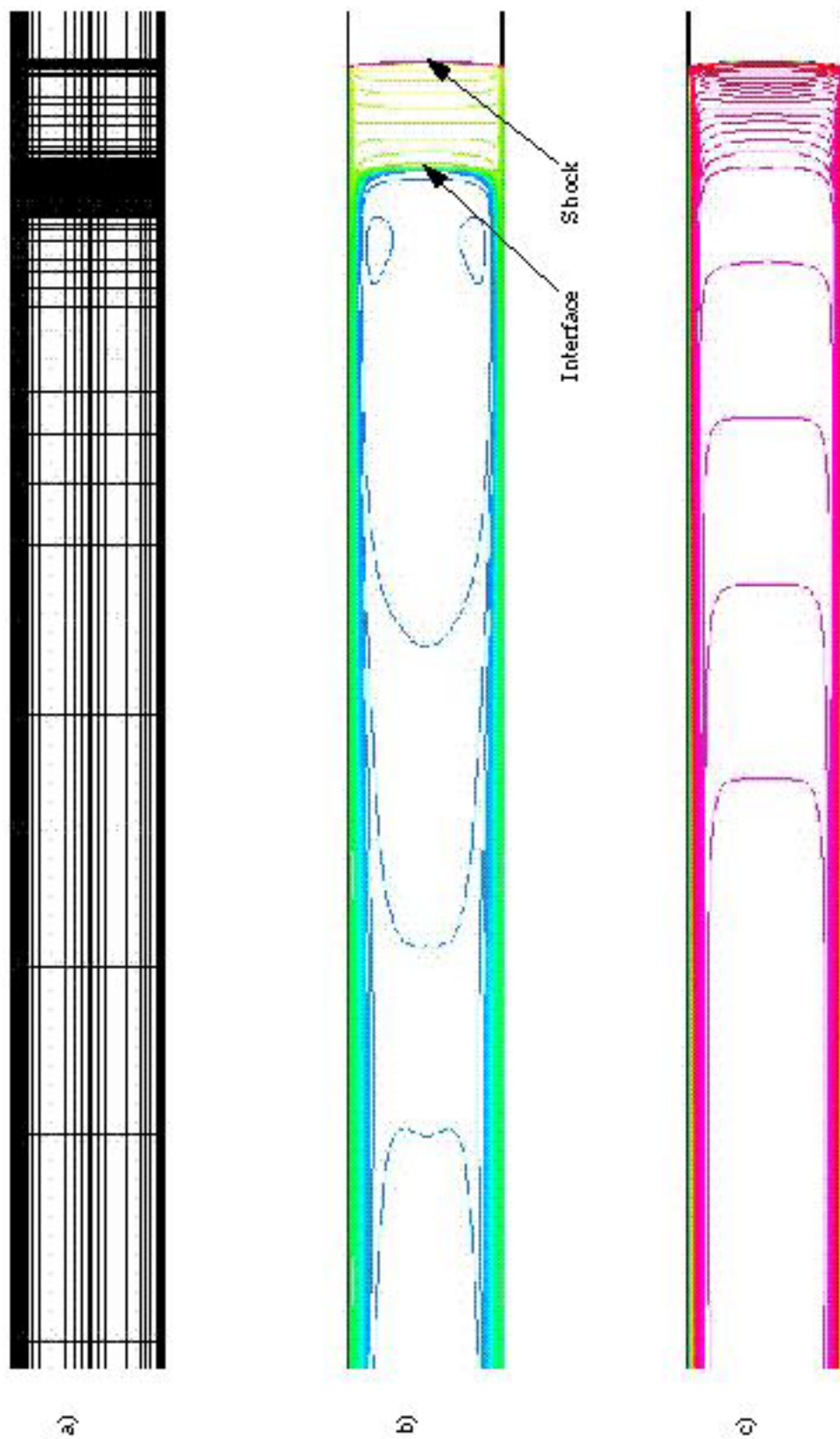


Figure 15. Flow solution for HYPULSE Mach 17 condition: a) grid (not all lines shown) b) density (log scale), c) u velocity component (40 m/sec per contour).

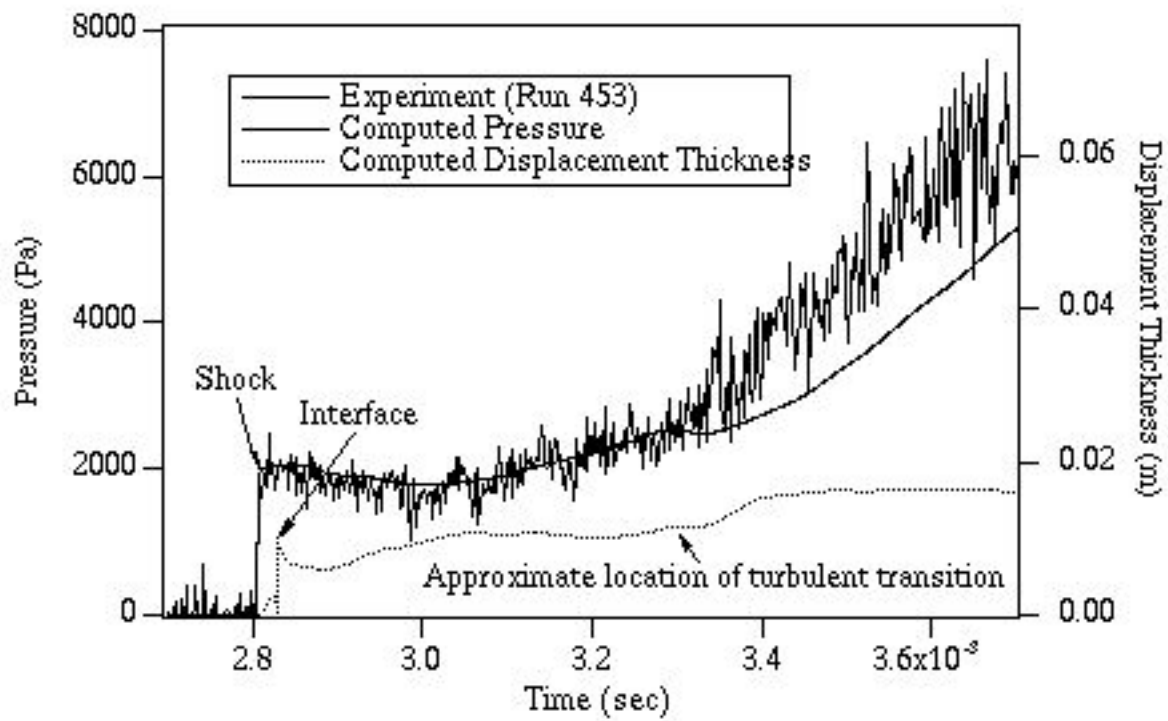


Figure 16. Computed and experimental pressure traces and computed displacement thickness at the end of the acceleration tube for the HYPULSE Mach 17 condition with transition to turbulence.

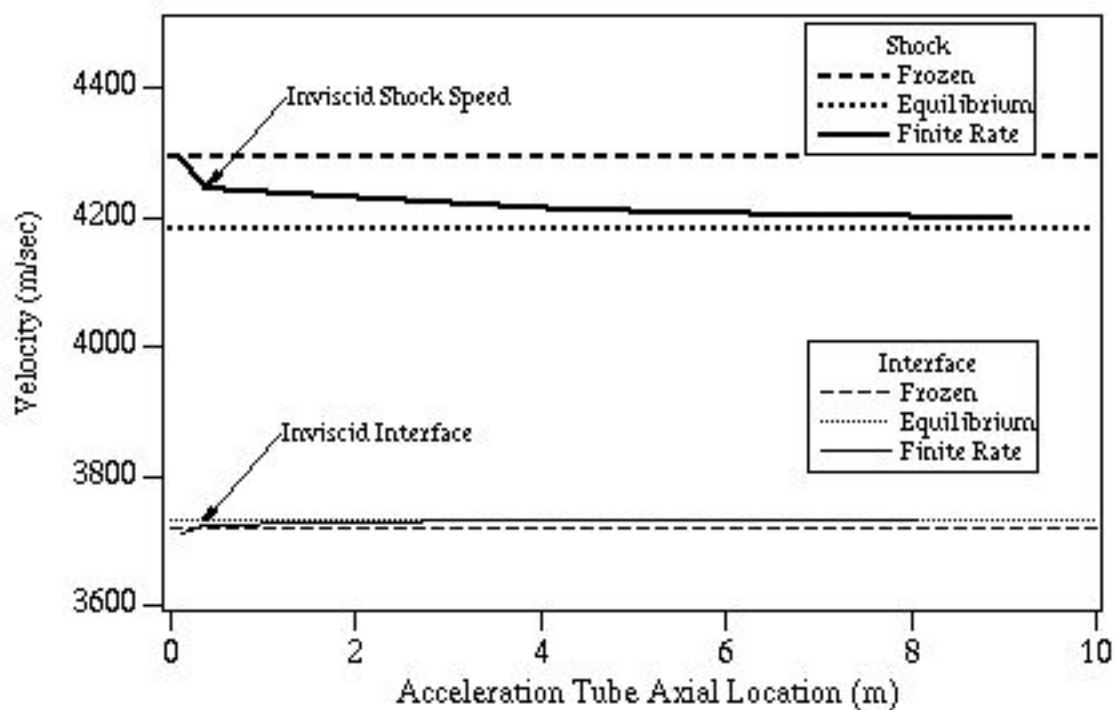


Figure 17. Computed shock speed versus distance in the acceleration tube for the inviscid simulation of the HYPULSE Mach 14 high-pressure condition showing the influence of finite-rate chemistry.



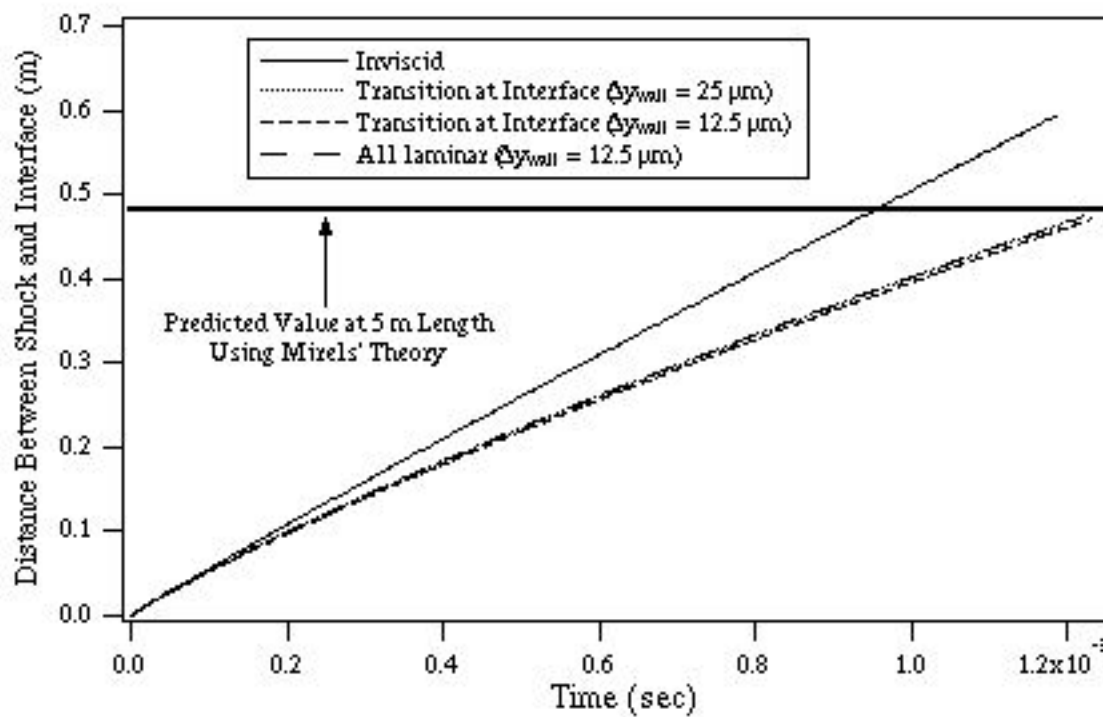


Figure 18. Computed distance between the shock and interface versus time for grid refinement study of the HYPULSE Mach 14 high-pressure condition using a 5 m acceleration tube.

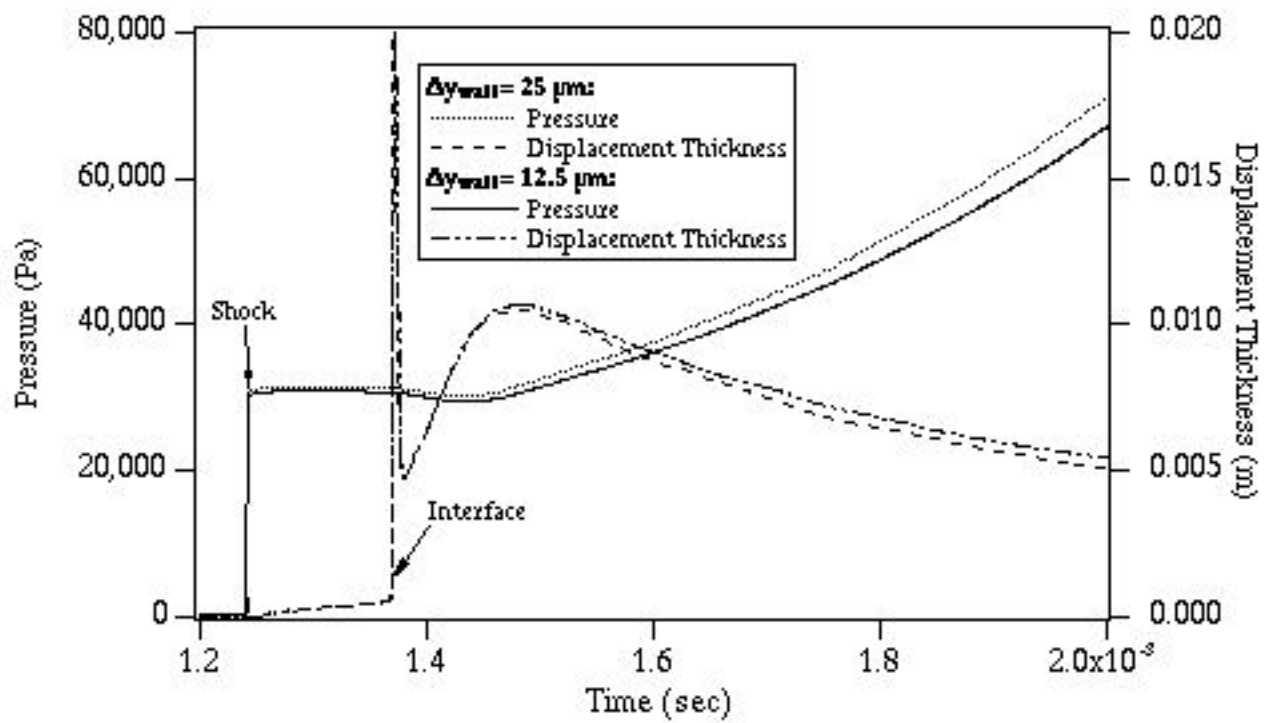


Figure 19. Computed pressure and displacement thickness for grid refinement study of the HYPULSE Mach 14 high-pressure condition.

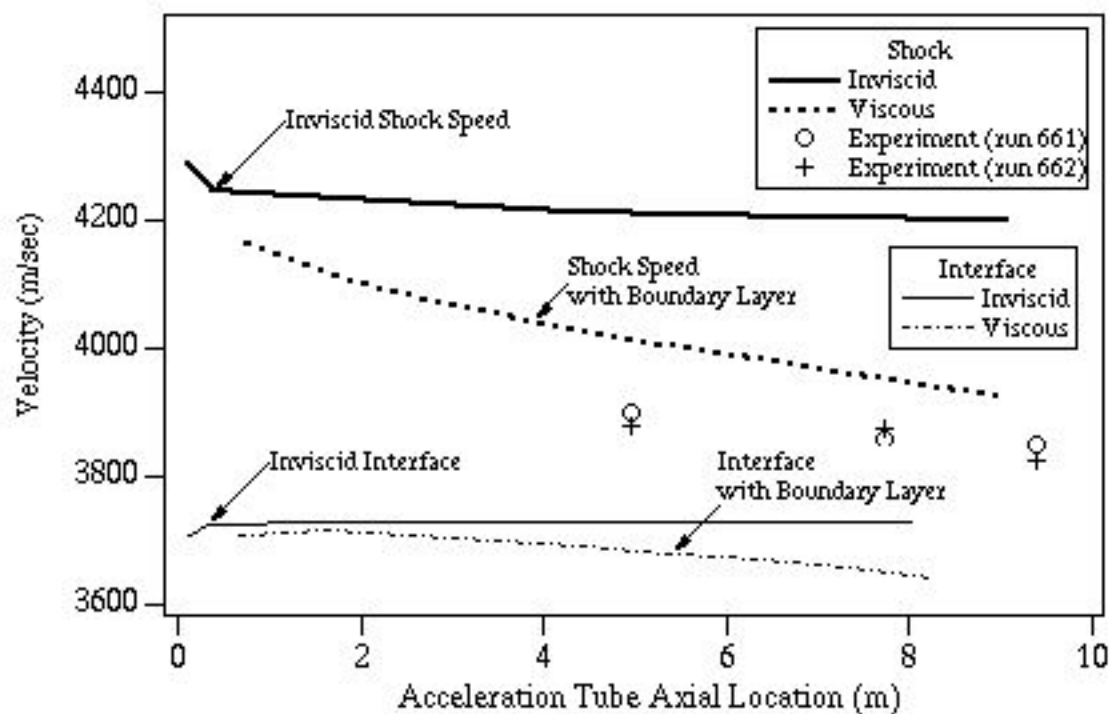


Figure 20. Computed and experimental shock speed versus distance in the acceleration tube for the HYPULSE Mach 14 high-pressure condition.

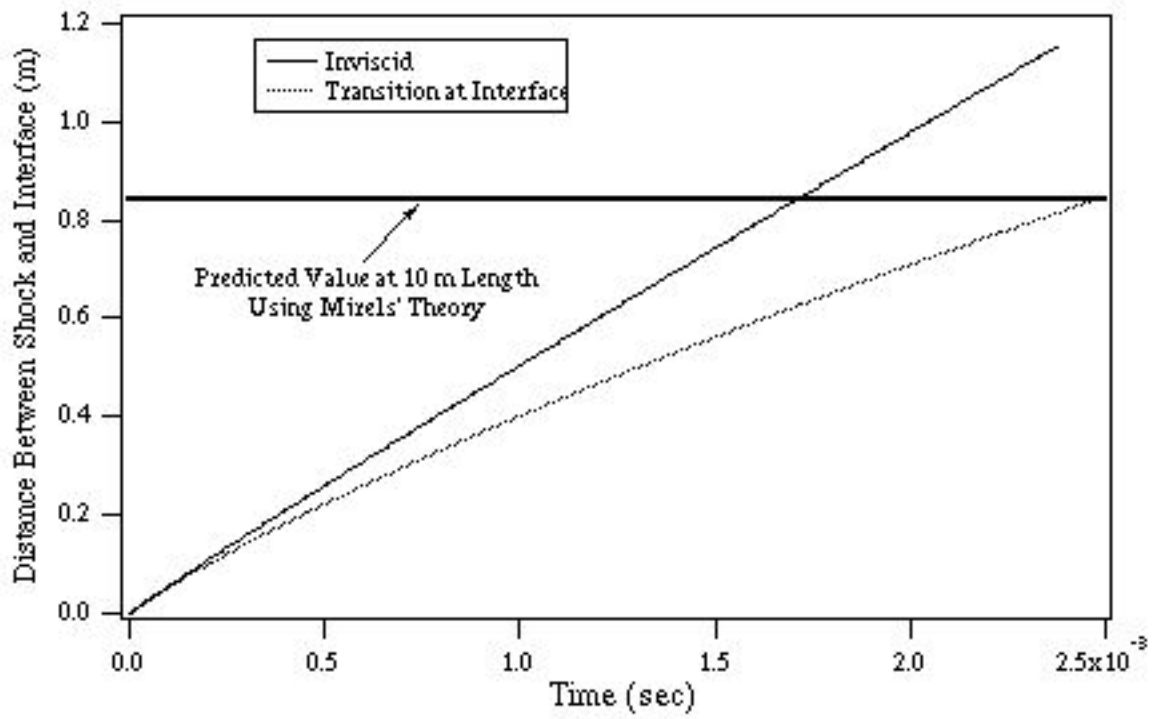


Figure 21. Computed distance between the shock and interface versus time for the HYPULSE Mach 14 high-pressure condition using a 10 m acceleration tube.

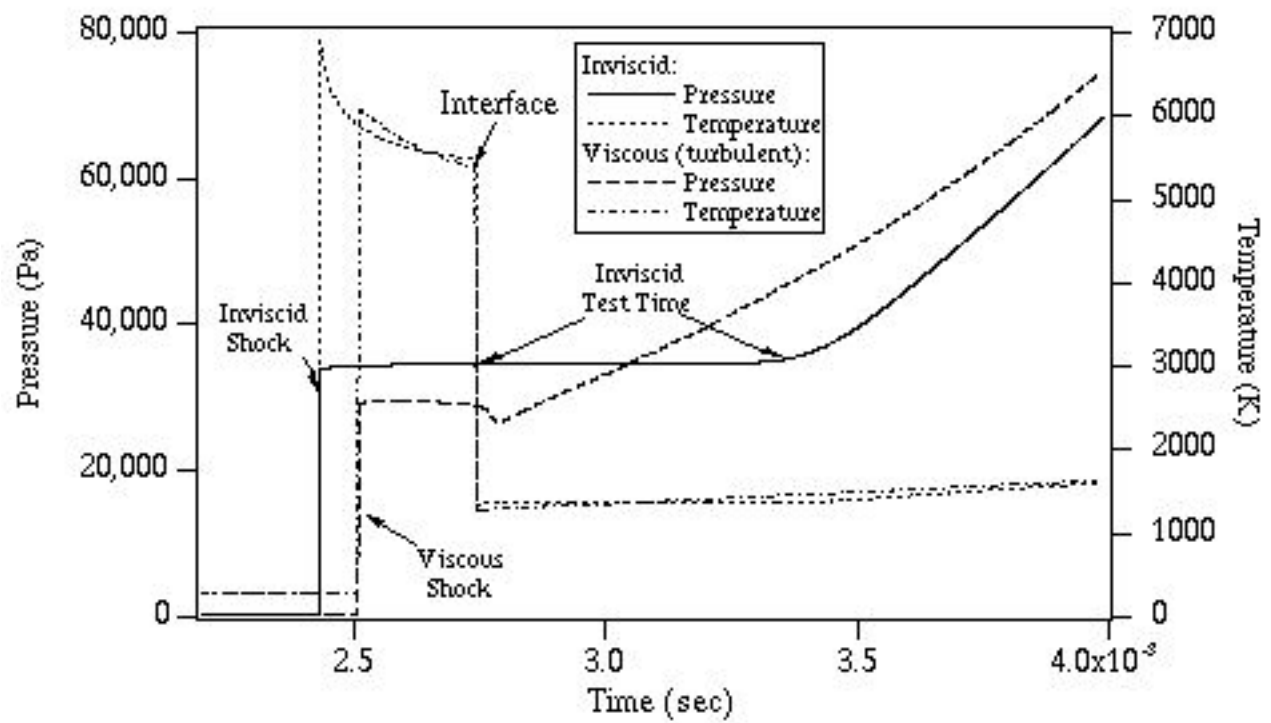


Figure 22. Computed pressure and temperature time traces at the end of the acceleration tube comparing inviscid and turbulent simulations of the HYPULSE Mach 14 high-pressure condition.

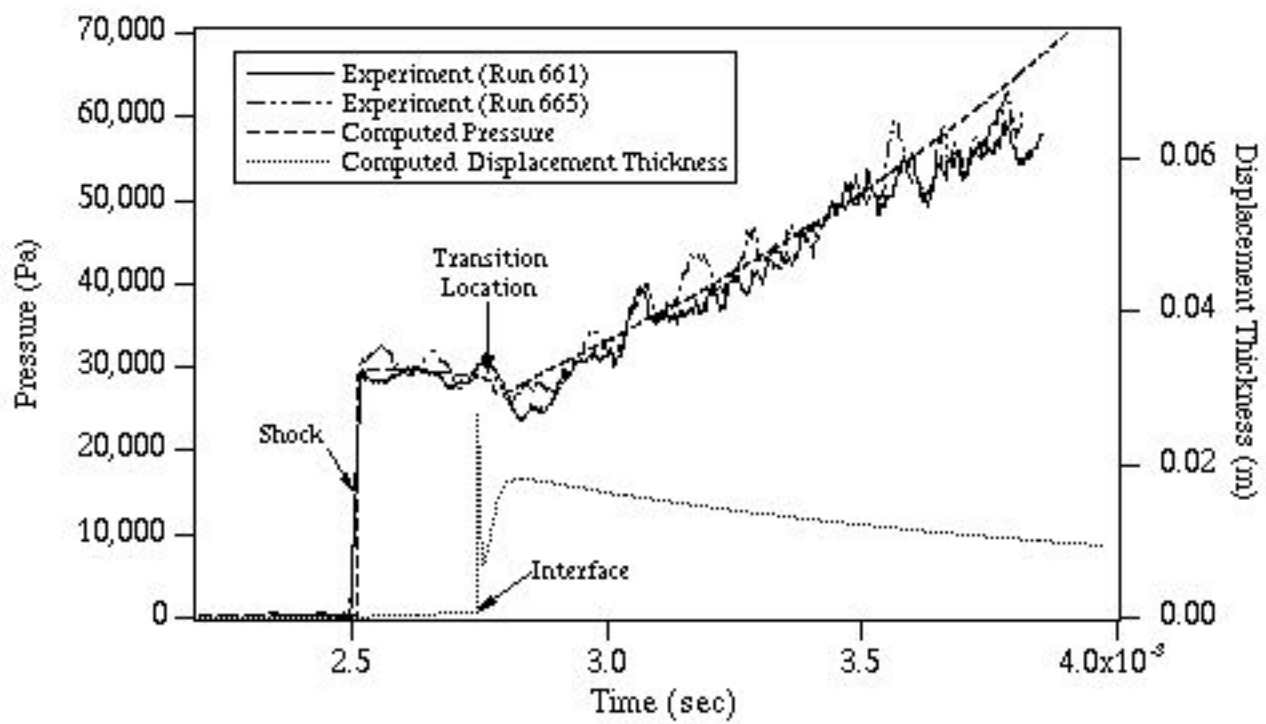


Figure 23. Computed and experimental pressure traces and computed displacement thickness at the end of the acceleration tube for the HYPULSE Mach 14 high-pressure condition.

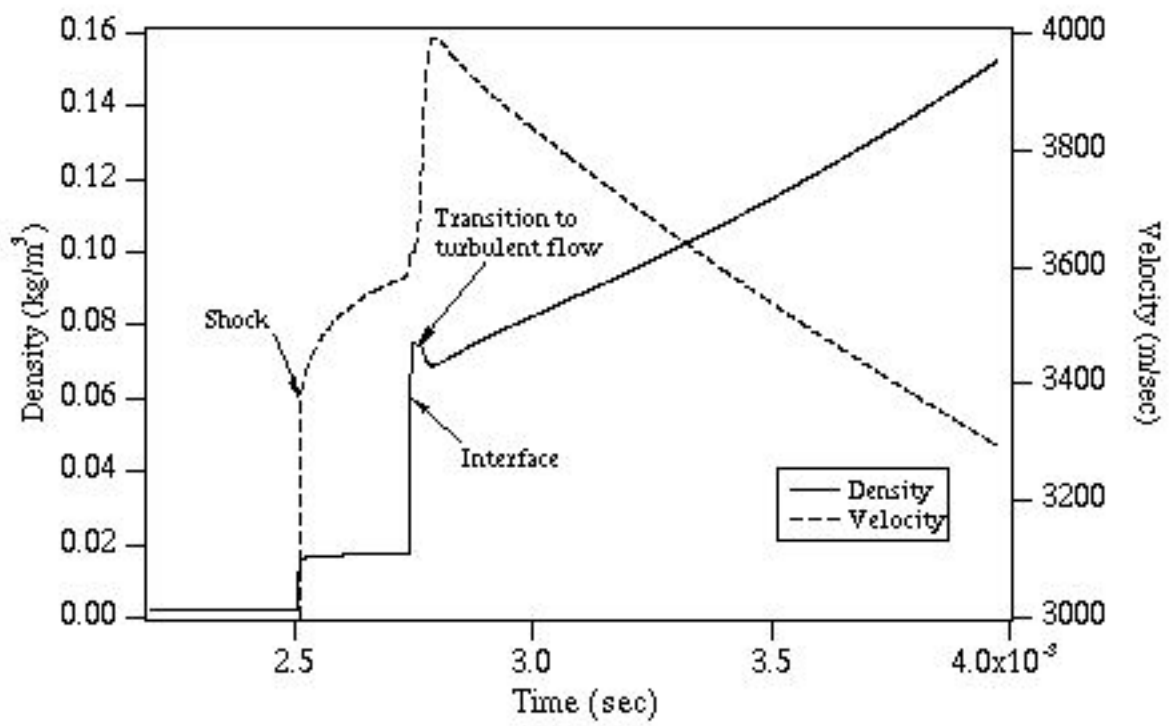


Figure 24. Computed density and velocity at the end of the acceleration tube for the HYPULSE Mach 14 high-pressure condition.

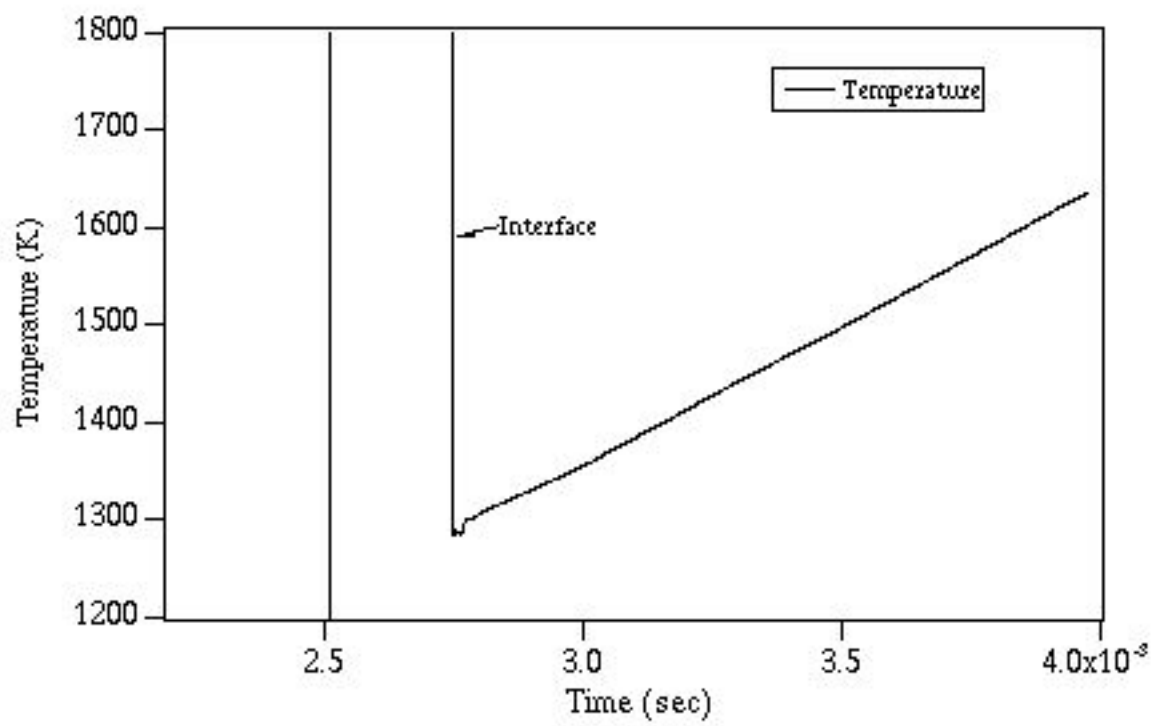


Figure 25. Computed temperature at the end of the acceleration tube for the HYPULSE Mach 14 high-pressure condition.



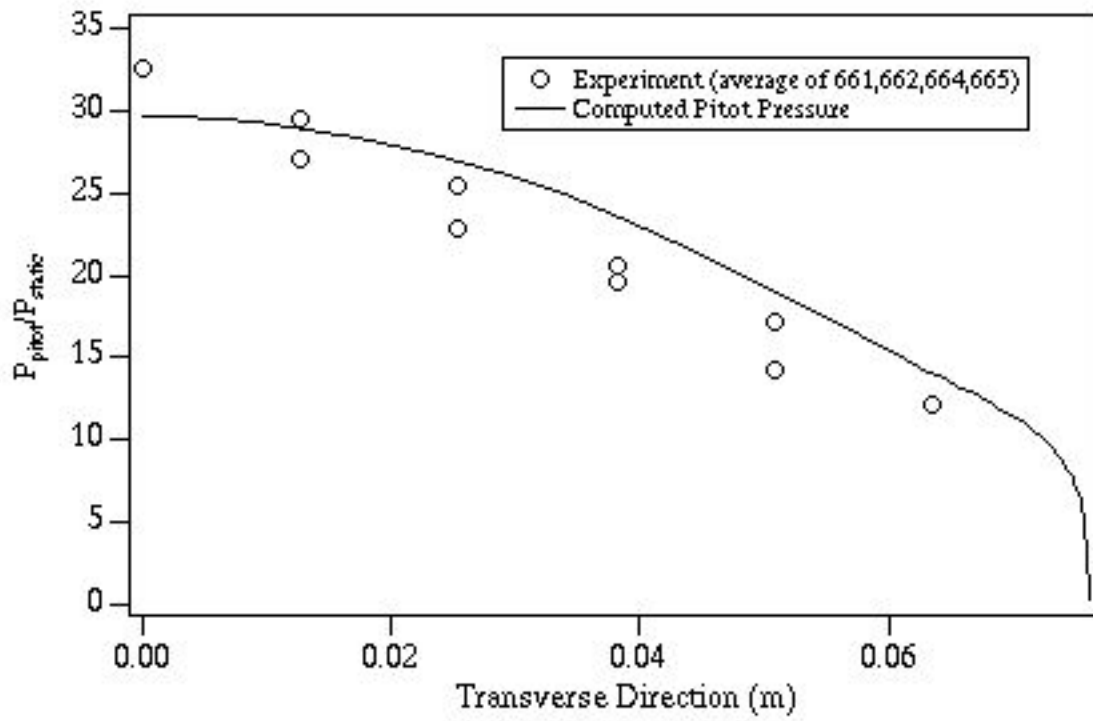
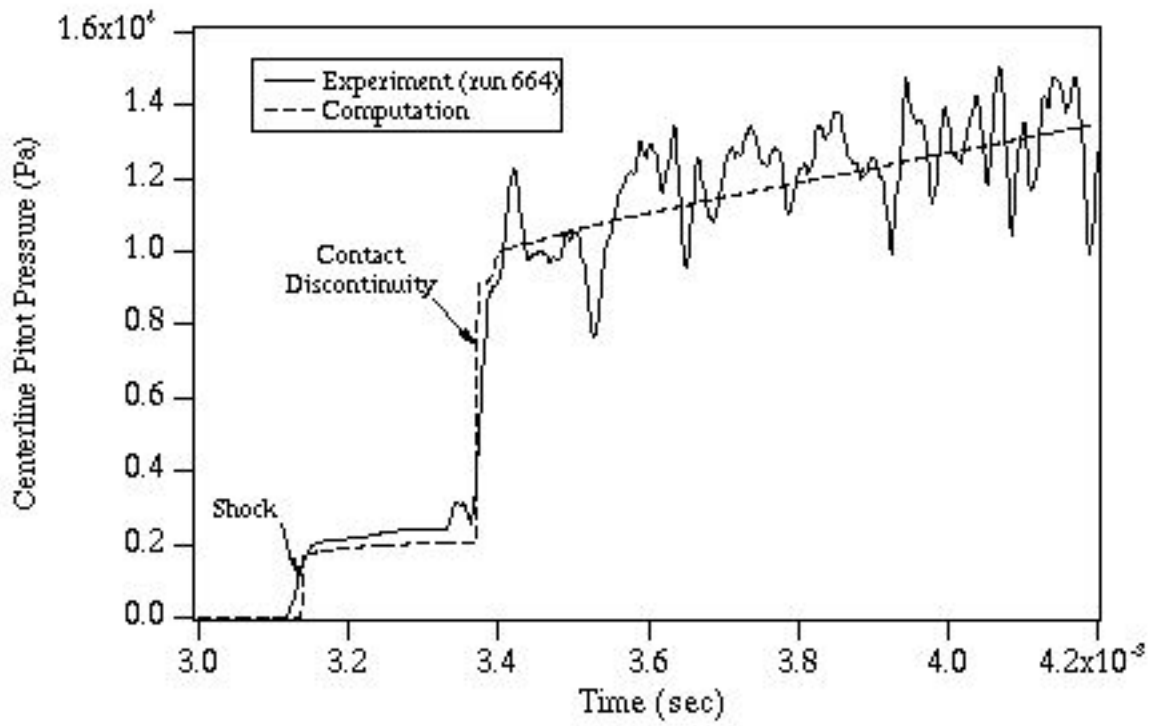
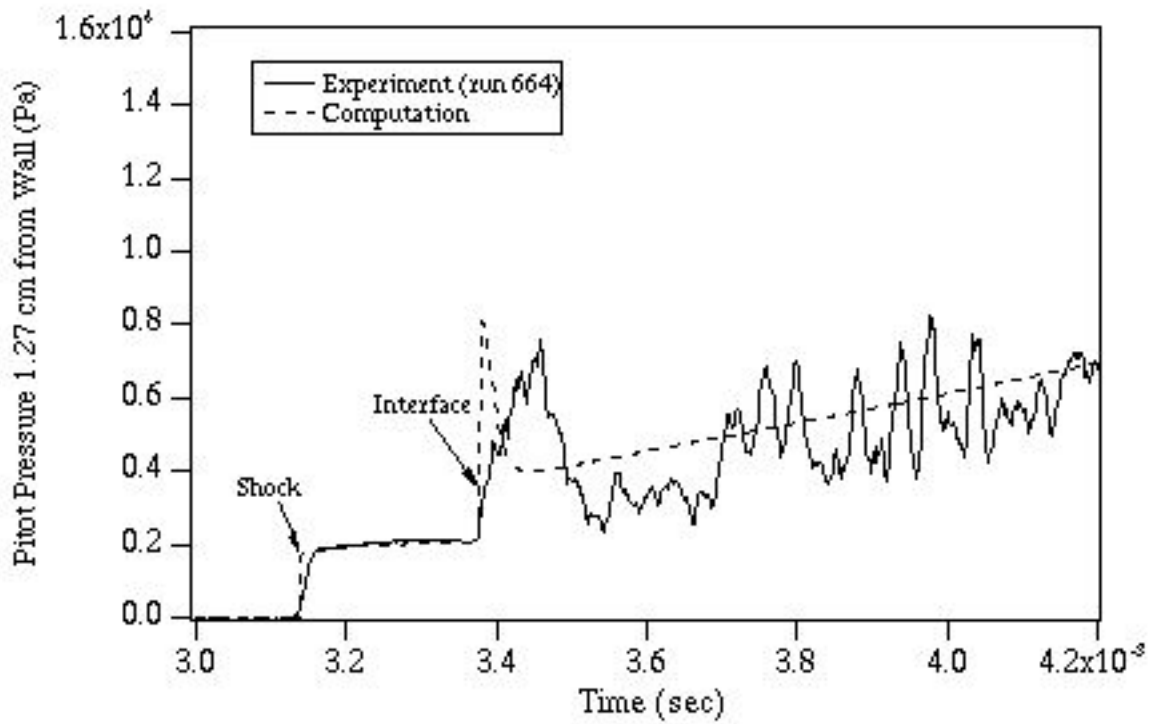


Figure 26. Computed and experimental pitot pressure profiles at the end of the acceleration tube for the HYPULSE Mach 14 high-pressure condition.



(a)



(b)

Figure 27. Computed and experimental pitot pressure traces at the end of the acceleration tube for the HYPULSE Mach 14 high-pressure condition: a) centerline b) 1.27 cm from wall.

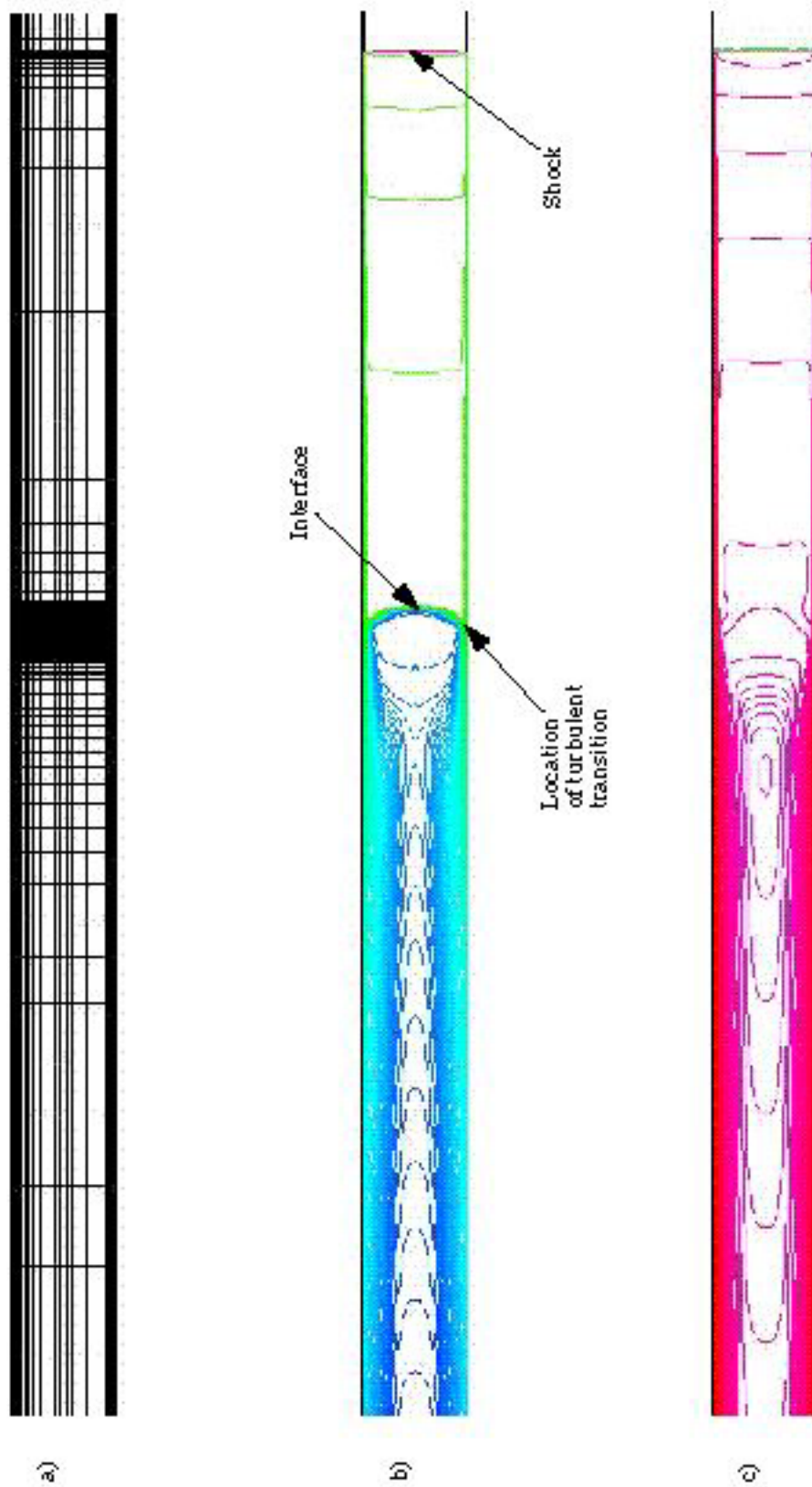


Figure 28. Flow solution for HYPULSE Mach 14 high-pressure condition: a) grid (not all lines shown) b) density (log scale) c) u velocity component (40 m/sec per contour).

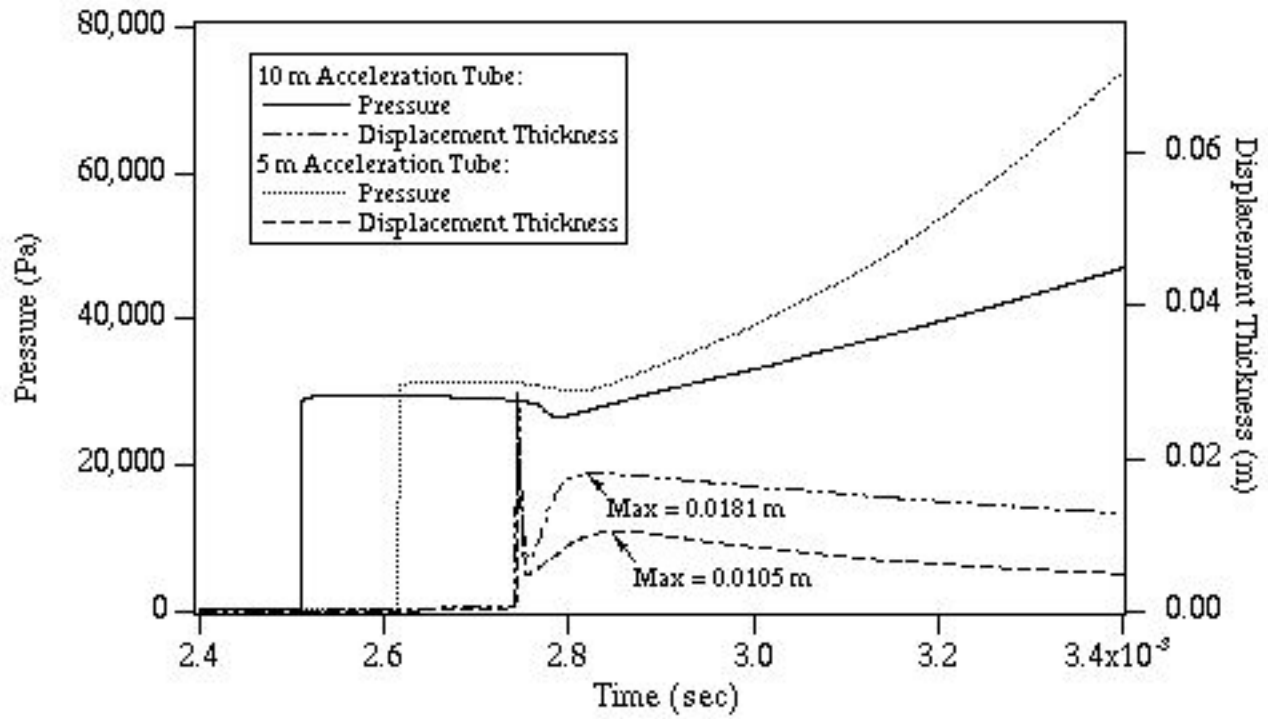


Figure 29. Computed pressure and displacement thickness at 5 m and 10 m along the acceleration tube for the HYPULSE Mach 14 high-pressure condition.

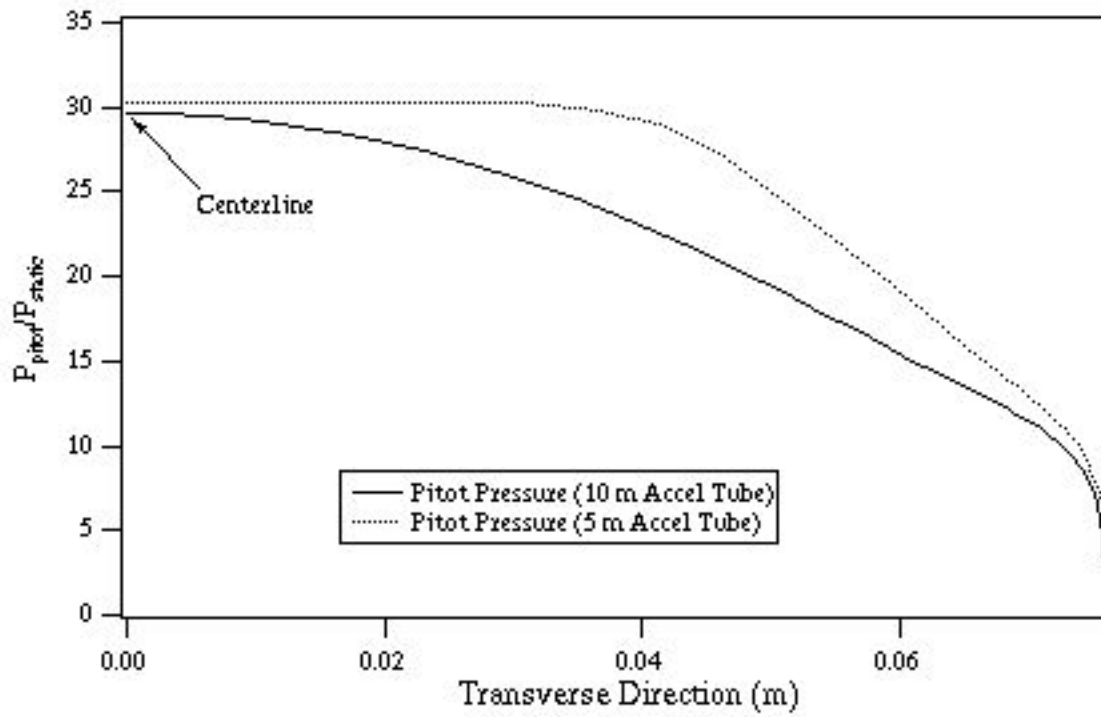


Figure 30. Computed pitot pressure profiles at 5 m and 10 m along the acceleration tube for the HYPULSE Mach 14 high-pressure condition.

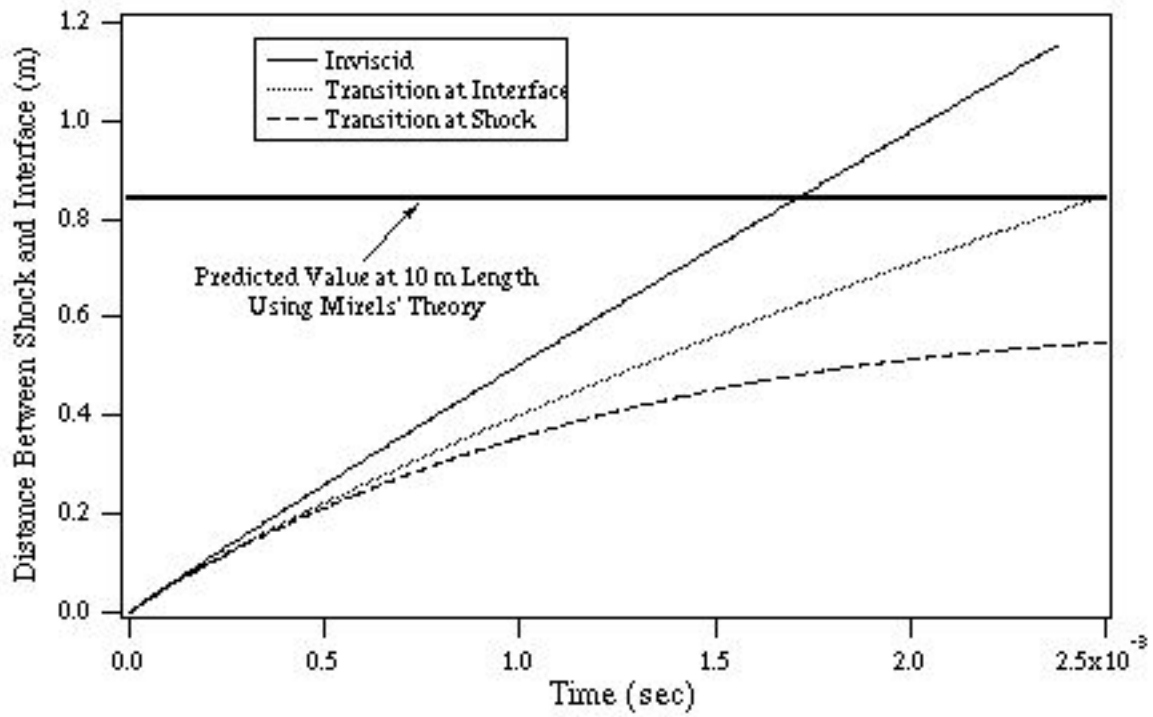


Figure 31. Computed distance between the shock and interface versus time for the HYPULSE Mach 14 high-pressure condition showing the influence of the turbulent transition location.

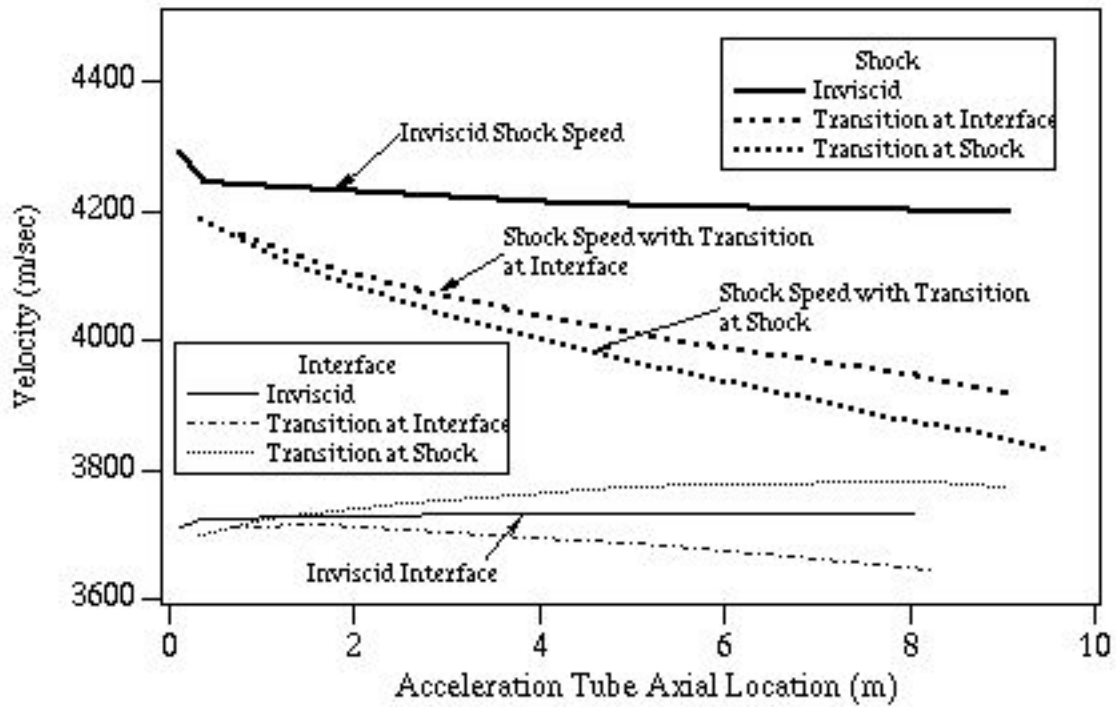


Figure 32. Computed shock and interface speed versus distance in the acceleration tube for the HYPULSE Mach 14 high-pressure condition showing the influence of the turbulent transition location.

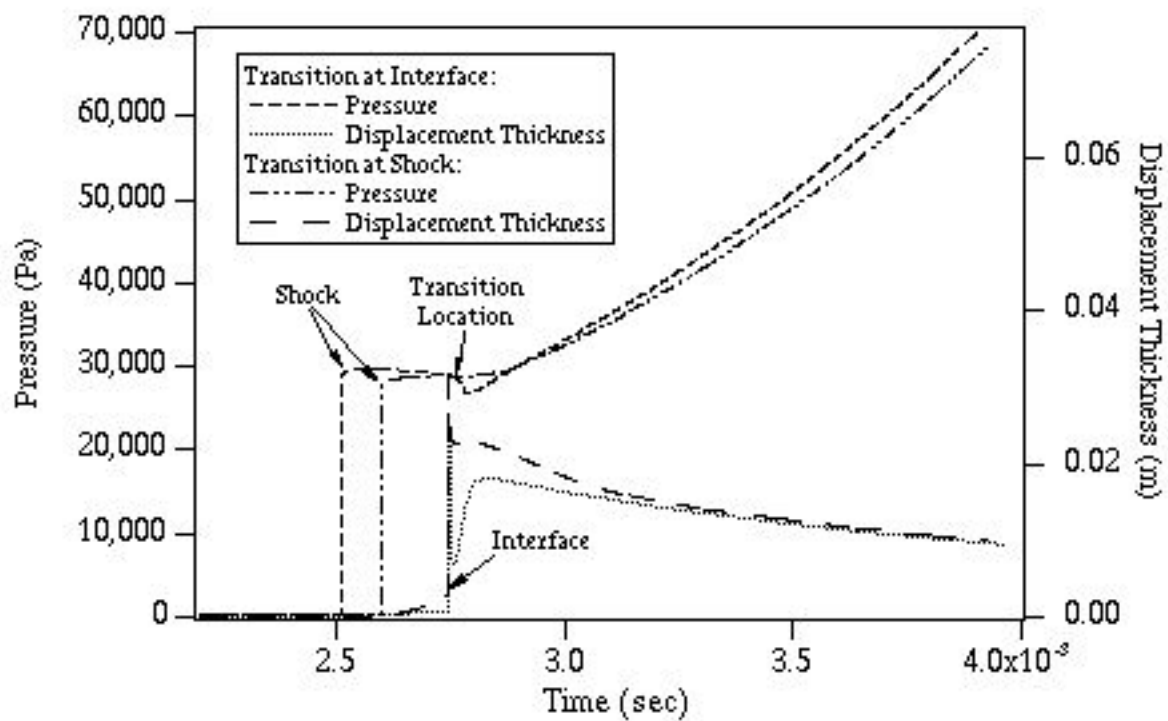


Figure 33. Computed pressure and displacement thickness for the HYPULSE Mach 14 high-pressure condition showing the influence of the turbulent transition location.



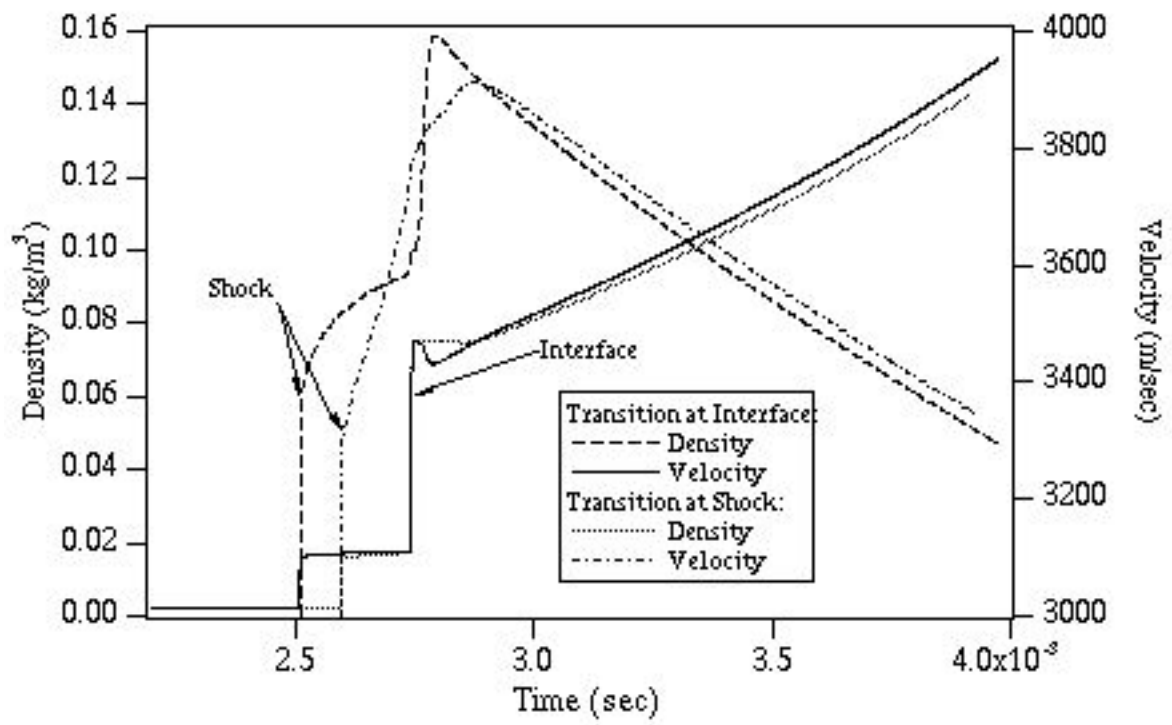


Figure 34. Computed density and velocity for the HYPULSE Mach 14 high-pressure condition showing the influence of the turbulent transition location.

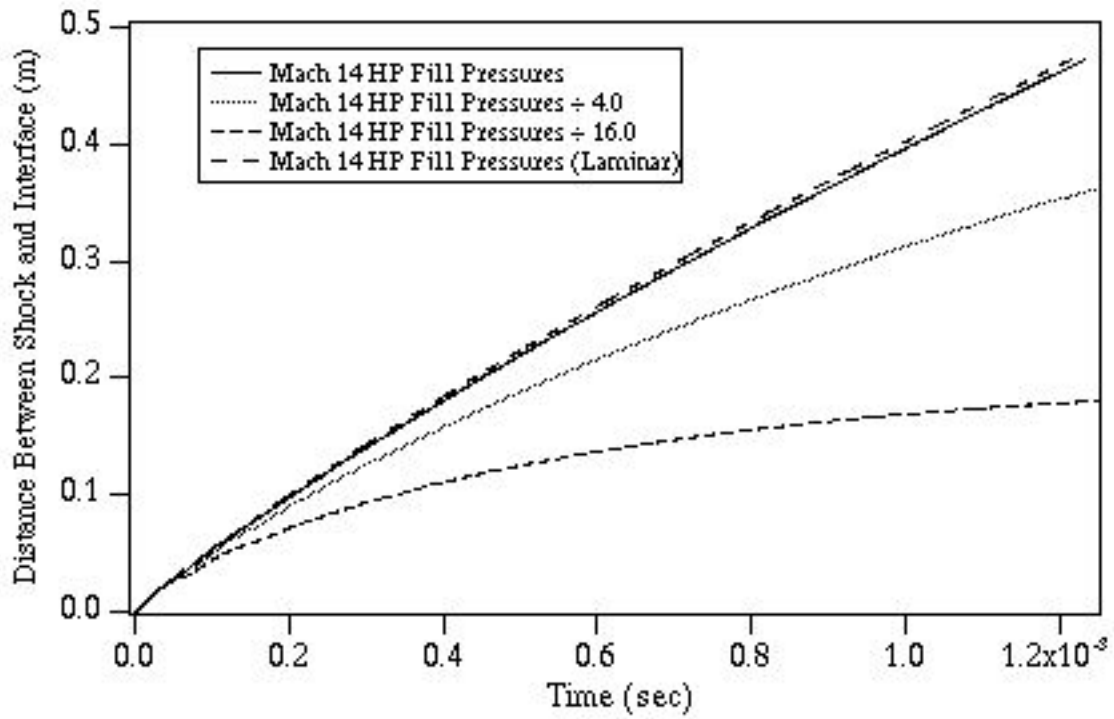


Figure 35. Computed distance between the shock and interface versus time for the HYPULSE Mach 14 high-pressure condition showing the influence of scaling the fill pressures.

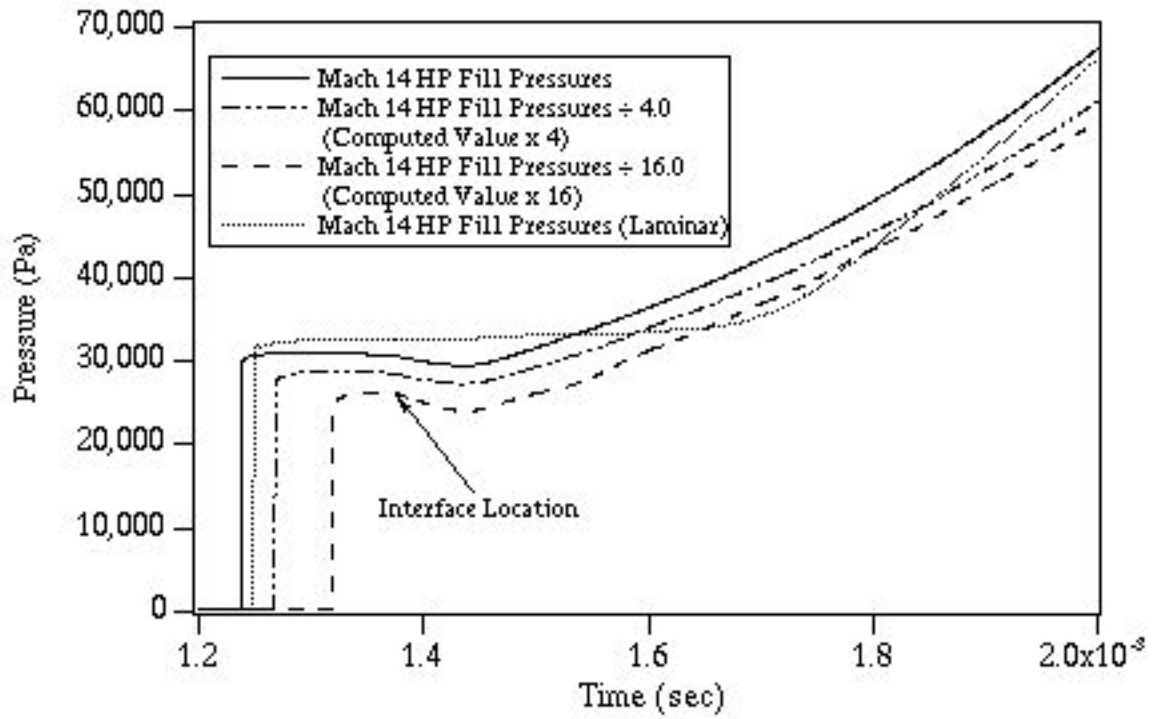


Figure 36. Computed pressure traces for the HYPULSE Mach 14 high-pressure condition showing the influence of scaling the fill pressures.

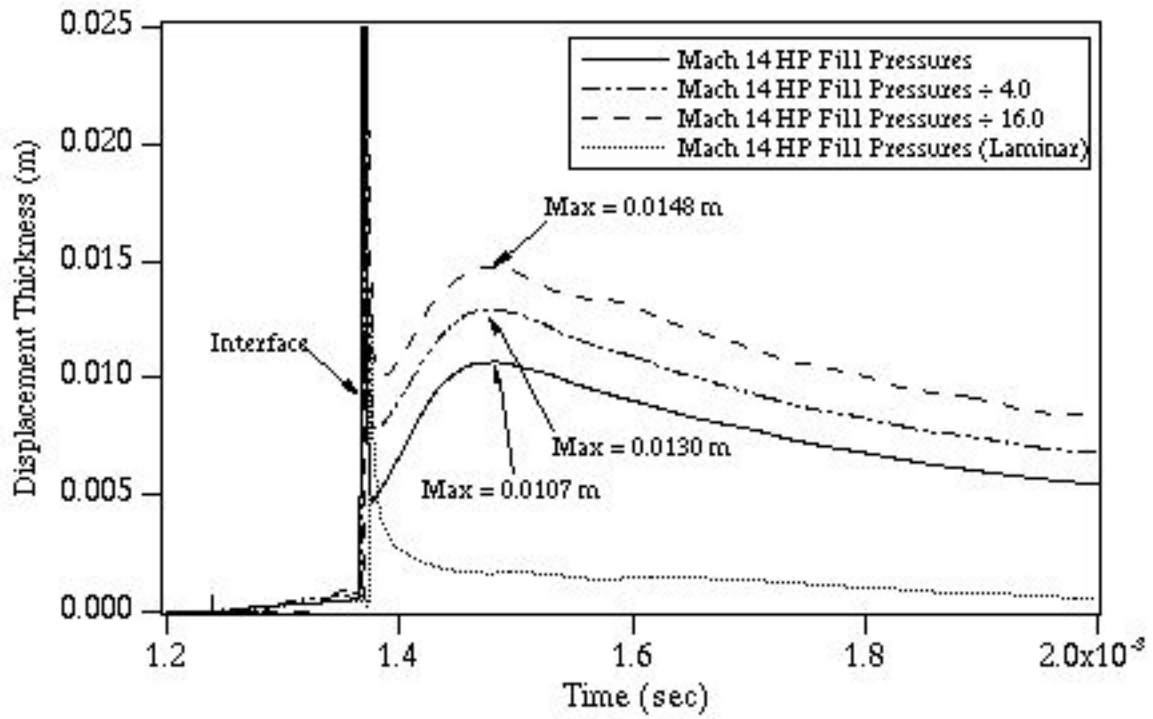


Figure 37. Computed displacement thickness for the HYPULSE Mach 14 high-pressure condition showing the influence of scaling the fill pressures.

<b>REPORT DOCUMENTATION PAGE</b>			Form Approved GSA No. 0704-0188	
Public reporting burden for this collection of information is estimated to average 1 hour per response, including the time for reviewing instructions, searching existing data sources, gathering and maintaining the data needed, and completing and reviewing the collection of information. Send comments regarding this burden estimate or any other aspect of this collection of information, including suggestions for reducing this burden, to Washington Headquarters Office, Directorate for Information Operations and Reports, 1215 Jefferson Davis Highway, Suite 1204, Arlington, VA 22202-4302, and to the Office of Management and Budget, Paperwork Reduction Project (0704-0188), Washington, DC 20503.				
1. AGENCY USE ONLY (Leave blank)		2. REPORT DATE June 1995		3. REPORT TYPE AND DATES COVERED Technical Memorandum
4. TITLE AND SUBTITLE Numerical Simulations of the Flow in the HYPULSE Expansion Tube			5. FUNDING NUMBERS  505-70-62	
6. AUTHOR(S)  Gregory J. Wilson, Myles A. Sussman, and Robert J. Bakos				
7. PERFORMING ORGANIZATION NAME(S) AND ADDRESS(ES) Thermosciences Institute Ames Research Center Moffett Field, CA 94035-1000			8. PERFORMING ORGANIZATION REPORT NUMBER  A-950072	
9. SPONSORING/MONITORING AGENCY NAME(S) AND ADDRESS(ES) National Aeronautics and Space Administration Washington, DC 20546-0001			10. SPONSORING/MONITORING AGENCY REPORT NUMBER  NASA TM-110357	
11. SUPPLEMENTARY NOTES Point of Contact: Gregory J. Wilson, Ames Research Center, MS 230-2, Moffett Field, CA 94035-1000; (415) 604-3472				
12a. DISTRIBUTION/AVAILABILITY STATEMENT  Unclassified-Unlimited Subject Category - 09			12b. DISTRIBUTION CODE	
13. ABSTRACT (Maximum 200 words) <i>Axisymmetric numerical simulations with finite-rate chemistry are presented for two operating conditions in the HYPULSE expansion tube. The operating gas for these two cases is nitrogen and the computations are compared to experimental data. One test condition is at a total enthalpy of 15.2 MJ/kg and a relatively low static pressure of 2 kPa. This case is characterized by a laminar boundary layer and significant chemical nonequilibrium in the acceleration gas. The second test condition is at a total enthalpy of 10.2 MJ/kg and a static pressure of 38 kPa and is characterized by a turbulent boundary layer. For both cases, the time-varying test gas pressure predicted by the simulations is in good agreement with experimental data. The computations are also found to be in good agreement with Mirels' correlations for shock tube flow. It is shown that the nonuniformity of the test gas observed in the HYPULSE expansion tube is strongly linked to the boundary layer thickness. The turbulent flow investigated has a larger boundary layer and greater test gas nonuniformity. In order to investigate possibilities of improving expansion tube flow quality by reducing the boundary layer thickness, parametric studies showing the effect of density and turbulent transition point on the test conditions are also presented. Although an increase in the expansion tube operating pressure level would reduce the boundary layer thickness, the simulations indicate that the reduction would be less than what is predicted by flat plate boundary layer correlations.</i>				
14. SUBJECT TERMS  Expansion tube, Computational fluid dynamics, Shock tube			15. NUMBER OF PAGES 53	
			16. PRICE CODE A04	
17. SECURITY CLASSIFICATION OF REPORT Unclassified	18. SECURITY CLASSIFICATION OF THIS PAGE Unclassified	19. SECURITY CLASSIFICATION OF ABSTRACT	20. LIMITATION OF ABSTRACT	